

THE EVOLUTION OF THE INTERSTELLAR MEDIUM IN POST-STARBURST GALAXIES

ZHIHUI LI,^{1,2,3,4} K. DECKER FRENCH,^{4,5} ANN I. ZABLUDOFF,⁴ AND LUIS C. HO^{2,3}

¹*Cahill Center for Astrophysics, California Institute of Technology, 1200 East California Boulevard, Pasadena, CA 91125, USA*

²*Kavli Institute for Astronomy and Astrophysics, Peking University, Beijing 100871, China*

³*Department of Astronomy, School of Physics, Peking University, Beijing 100871, China*

⁴*Steward Observatory, University of Arizona, 933 North Cherry Avenue, Tucson AZ 85721*

⁵*Observatories of the Carnegie Institution for Science, 813 Santa Barbara Street, Pasadena CA 91101*

ABSTRACT

We derive dust masses (M_{dust}) from the spectral energy distributions of 58 post-starburst galaxies (PSBs). There is an anti-correlation between specific dust mass ($M_{\text{dust}}/M_{\star}$) and the time elapsed since the starburst ended, indicating that dust was either destroyed, expelled, or rendered undetectable over the ~ 1 Gyr after the burst. The $M_{\text{dust}}/M_{\star}$ depletion timescale, 205^{+58}_{-37} Myr, is consistent with that of the CO-traced M_{H_2}/M_{\star} , suggesting that dust and gas are altered via the same process. Extrapolating these trends leads to the $M_{\text{dust}}/M_{\star}$ and M_{H_2}/M_{\star} values of early-type galaxies (ETGs) within 1-2 Gyr, a timescale consistent with the evolution of other PSB properties into ETGs. Comparing M_{dust} and M_{H_2} for PSBs yields a calibration, $\log M_{\text{H}_2} = 0.45 \log M_{\text{dust}} + 6.02$, that allows us to place 33 PSBs on the Kennicutt-Schmidt (KS) plane, $\Sigma\text{SFR} - \Sigma M_{\text{H}_2}$. Over the first ~ 200 -300 Myr, the PSBs evolve down and off of the KS relation, as their star formation rate (SFR) decreases more rapidly than M_{H_2} . Afterwards, M_{H_2} continues to decline whereas the SFR levels off. These trends suggest that the star-formation efficiency bottoms out at 10^{-11} yr^{-1} and will rise to ETG levels within 0.5-1.1 Gyr afterwards. The SFR decline after the burst is likely due to the absence of gas denser than the CO-traced H_2 . The mechanism of the $M_{\text{dust}}/M_{\star}$ and M_{H_2}/M_{\star} decline, whose timescale suggests active galactic nucleus (AGN) or low-ionization nuclear emission-line region (LINER) feedback, may also be preventing the large CO-traced molecular gas reservoirs from collapsing and forming denser star forming clouds.

Keywords: galaxies: evolution — galaxies: ISM — galaxies: starburst — infrared: galaxies

arXiv:1906.01890v2 [astro-ph.GA] 17 Jun 2019

1. INTRODUCTION

Lying in the ‘green valley’ (Wong et al. 2012) of the galaxy color-magnitude diagram, post-starburst (PSB) galaxies (Dressler & Gunn 1983) is a transitioning phase between star-forming spirals and gas-poor quiescent galaxies (Yang et al. 2004, 2008, and references therein). The absence of significant nebular emission lines (e.g., [O II], H α) is indicative of little-to-no ongoing star formation. However, the presence of strong Balmer absorption reveals young and recently formed A-stars (Dressler & Gunn 1983; Couch & Sharples 1987). These signatures indicate a recent starburst within the last \sim Gyr. Although PSBs are a rare species at almost all redshifts ($<1\%$ by $z \sim 0.5$, Wild et al. 2016), the shortness of the PSB phase suggests that a large fraction (25-40%) of field galaxies at $z < 1$ may have passed through it (Zabludoff et al. 1996; Tran et al. 2004; Snyder et al. 2011). Thus, PSBs are important to understanding the evolutionary path from star-forming galaxies to early-type galaxies (ETGs).

Over the past decade, many attempts have been made to study the interstellar medium (ISM) properties of PSBs. The existence of atomic gas (HI) has been confirmed in several small samples of PSBs (e.g., Chang et al. 2001; Buyle et al. 2006; Zwaan et al. 2013). Recent work has also revealed the existence of large molecular gas (H $_2$) reservoirs in PSBs (e.g., French et al. 2015; Rowlands et al. 2015). French et al. (2018a) even discovered that the CO-traced H $_2$ declines with post-burst age over a timescale that would lead to ETG levels in 0.7-1.5 Gyr. However, as obtaining gas masses requires large amounts of radio telescope time, these studies are limited to small sample sizes. Alternatively, dust mass (M_{dust}) can be used to track the ISM evolution for a larger sample of PSBs, as it is more easily measured, i.e., by fitting the galaxy’s spectral energy distributions (SED) over mid-infrared (MIR) to far-infrared (FIR) wavelengths. Archival data are now available for a statistically significant PSB sample, making it possible to calibrate the relation between M_{dust} and CO-traced M_{H_2} for the first time, as well as to examine the evolution of M_{dust} over a wide range of post-burst ages.

Smercina et al. (2018) derived M_{dust} for 33 PSBs with CO detections from French et al. (2015) and investigated the evolution of their ISM properties in detail. In contrast, here we search all available archival IR data for three large PSB samples from French et al. (2018a), Alatalo et al. (2016a), and Rowlands et al. (2015) and derive M_{dust} for those 58 PSBs with sufficient IR data. Thus, we study the evolution of M_{dust} with a larger sample size and a wider age baseline.

As Kennicutt (1998) points out, there is a universal correlation between the surface density of gas and star formation rate (SFR) for local normal star-forming galaxies and starburst galaxies (the Kennicutt-Schmidt relation, or the KS relation). For a sample of PSBs, French et al. (2015) observed a

significant offset from the KS relation. But what is the evolutionary track for PSBs in the KS plane? The tight correlation between gas and dust that we observe here makes it possible for us to map this evolution for the first time and to connect it to changes in the star formation efficiency (SFE).

In this paper, we derive M_{dust} for 58 PSBs by performing ultraviolet (UV) to FIR SED fitting. We study the evolution of M_{dust} and SFE after the burst ends. We also investigate the dust-derived KS relation. In Section 2, we summarize our PSB sample selection criteria. In Section 3, we describe the archival fluxes and errors used to construct full SED of our sample. In Section 4, we discuss the CIGALE-based (Code Investigating GALaxy Emission; Noll et al. 2009; Boquien et al. 2019) SED fitting procedure and present the results. In Section 5, we consider the evolution of M_{dust} , the position on the KS plane, and the SFE of our PSB sample. Section 6 lists our conclusions. Throughout this paper we adopt a flat Λ CDM cosmology with $\Omega_m = 0.308$, $\Omega_\Lambda = 0.692$, and $H_0 = 67.8 \text{ km s}^{-1} \text{ Mpc}^{-1}$ (Planck Collaboration et al. 2016).

2. SAMPLE SELECTION

In this work, we combine three well-studied PSB samples from French et al. (2018a), Alatalo et al. (2016a), and Rowlands et al. (2015) to make the time baseline since the starburst ends as wide as possible. Our combined PSB sample ranges in post-burst age from \sim -100 to \sim 800 Myr, which enables us to sample any significant trends. The general idea of constructing PSB samples is requiring strong Balmer absorption lines (suggesting recent starbursts), and weak nebular emission (indicating little ongoing star formation). Specifically, French et al. (2018a) use $\text{H}\delta_A - \sigma(\text{H}\delta_A) > 4 \text{ \AA}$ (where $\sigma(\text{H}\delta_A)$ is the measurement error of the $\text{H}\delta_A$ index) and $\text{H}\alpha$ rest-frame equivalent width, $\text{EW}(\text{H}\alpha) < 3 \text{ \AA}$ as their selection criteria, which yield a sample of real *post*-starburst galaxies. Alatalo et al. (2016a) allow for emission lines from shocks and use $\text{H}\delta_A > 5 \text{ \AA}$ after emission-line correction; as this emission also may arise from star formation, their sample could still have ongoing starbursts. These objects turn out to be at earlier PSB stages, while some even have negative post-burst ages, signifying an ongoing burst (French et al. 2018a). Thus, they serve as crucial links between the cessation of the recent burst and the subsequent decline in star formation. Rowlands et al. (2015) use a Principal Component Analysis (PCA) technique at 3175 – 4150 \AA , which essentially requires strong Balmer absorption and weak 4000 \AA break strength; such a selection focuses on young stellar ages and thus, like the Alatalo et al. (2016a) sample, includes transitioning galaxies from a starbursting to PSB phase.

One of the primary goals of our work here is to derive M_{dust} . As previous studies have shown that FIR ($\lambda \geq 40\mu\text{m}$) photometry is crucial (da Cunha et al. 2008; Dale et al. 2012), we define our sample as those galaxies among the aforemen-

tioned three samples of PSBs with archival FIR data. In addition to utilizing the processed *WISE* and *Herschel* data from [Smercina et al. \(2018\)](#) for 33 PSBs from [French et al. \(2015\)](#), we searched for *Herschel* observations of other galaxies in these three samples in the PACS Point Source Catalog ([Martin et al. 2017](#)) and SPIRE Point Source Catalog ([Schulz et al. 2017](#)), available at the NASA/IPAC Infrared Science Archive (IRSA)¹. As a result, 37 PSBs from [French et al. \(2018a\)](#), 12 PSBs from [Alatalo et al. \(2016a\)](#), and 11 PSBs from [Rowlands et al. \(2015\)](#) have detections in ≥ 3 *Herschel* bands², constituting our final sample of 58 PSBs in total³. The 37 PSBs from [French et al. \(2018a\)](#) are labeled EAH01-EAH18 and EAS01-EAS15, consistent with the nomenclature in [French et al. \(2015\)](#) and [Smercina et al. \(2018\)](#), and F34-F37, for those without previous names. Their redshifts are $0.02 < z < 0.11$. The 12 PSBs from [Alatalo et al. \(2016a\)](#) are A1-A12, with $0.02 < z < 0.18$. The 11 PSBs from [Rowlands et al. \(2015\)](#) are R1-R11, with $0.03 < z < 0.05$.

3. MULTIWAVELENGTH DATA

We establish UV to FIR SEDs for our PSB sample. We incorporate the processed *WISE* and *Herschel* data from [Smercina et al. \(2018\)](#) for 33 PSBs from [French et al. \(2015\)](#) and compile other data from different catalogs. In addition to compiling the *Herschel* data from PACS/SPIRE Point Source Catalogs, we utilize the archival photometric data from *GALEX*, SDSS, 2MASS, and *WISE*. We have also calculated the flux uncertainties by combining in quadrature the cataloged measurement uncertainties with different systematic uncertainties in each band, which are described individually in the following paragraphs.

For *GALEX* data, we search for NUV and FUV detections from the *GALEX* All-Sky Survey Source Catalog (GASC) and the Medium Imaging Survey Catalog (GMSC)⁴. We use the `mag_FUV` and `mag_NUV` magnitudes, which should be representative of the total galaxy flux. We further add zero-point calibration errors of 0.052 and 0.026 mag to the FUV and NUV photometry errors, respectively ([Morrissey et al. 2007](#)).

For SDSS data, we search for *ugriz* photometry in the `Photoobjall` catalog of the SDSS 14th Data Release (DR14, [Abolfathi et al. 2018](#)). We adopt the `modelmag` magnitudes, as they provide reliable colors and represent the total light of our sources⁵. To ensure all the magnitudes are

on the AB system, we add -0.04 to measured *u*-band magnitudes and 0.02 to *z*-band magnitudes⁶. Zero-point calibration errors of 5%, 2%, 2%, 2%, and 3% are added to the photometry errors of *ugriz* bands, respectively ([Blanton & Roweis 2007](#)).

For 2MASS data, we search for *JHK_s* photometry from the 2MASS Point Source Catalog (PSC; [Skrutskie et al. 2006](#)) and Extended Source Catalog (XSC; [Jarrett et al. 2000](#)). If the source is cataloged in PSC, we adopt the standard aperture, which is measured in a 4'' radius aperture, but has already been corrected to an infinite aperture. If the source is cataloged in XSC, we choose the extrapolated total magnitude `x_m_ext`, which should represent the total flux⁷. We convolve a 5% calibration error ([Dale et al. 2009](#)) with the photometry error in quadrature.

For *WISE* data, we search for *W1-W4* photometry in the ALLWISE Source Catalog ([Mainzer et al. 2011](#)). We use the magnitudes measured with profile-fitting photometry (`wxmp`) for point sources (defined with `ext_flg = 0`). For extended sources (`ext_flg > 0`), we follow the instructions from the *WISE* official website⁸: when `ext_flg = 5`, we adopt the `wxgmag` measured with an elliptical aperture; when $0 < \text{ext_flg} < 5$, we choose the circular aperture magnitude that best matches the extrapolated total radius `r_ext` provided in 2MASS. We correct zero-point errors by adding 0.03, 0.04, 0.03, and -0.03 mag to the measured *WISE* *W1-W4* bands, respectively ([Jarrett et al. 2012](#)). We add an overall 6% calibration error for the *W1-W4* bands to the photometry error ([Cutri et al. 2015](#)).

For *Herschel* data, we adopt the quantity `flux` from the PACS/SPIRE Point Source Catalogs. The PACS flux uncertainties are derived by convolving the `snrnoise` (including sky confusion and instrumental error) and the background `rms`. The SPIRE ‘total’ flux uncertainties `flux_err` include instrumental noise and background confusion noise. We add a 7% calibration error to the PACS and SPIRE flux uncertainties ([Ciesla et al. 2012](#); [Balog et al. 2014](#)).

All the data are presented in Tables 2 and 3. We do not apply any correction for Galactic extinction, because it is only nonnegligible for several sources and only affects the UV and optical data, which do not affect M_{dust} (see Appendix B). To characterize the amount of internal extinction, we have incorporated the [Calzetti et al. \(2000\)](#) law into our SED fitting (Section 4.1).

4. SED FITTING

In this work, we perform UV-FIR SED fitting on our sample using CIGALE (Code Investigating GALaxy Emission;

¹ <http://irsa.ipac.caltech.edu/>.

² We will justify the necessity of using at least three *Herschel* bands in Appendix A.

³ Two objects (R8/A11 and R11/A12) are in both the [Alatalo et al. \(2016a\)](#) and [Rowlands et al. \(2015\)](#) samples, and we refer to them as A11 and A12 in this paper.

⁴ <http://galex.stsci.edu/galexview/>.

⁵ <http://www.sdss.org/dr14/algorithms/magnitudes/>.

⁶ <http://www.sdss.org/dr14/algorithms/fluxcal/>.

⁷ https://www.ipac.caltech.edu/2mass/releases/allsky/doc/sec4_5e.html.

⁸ <http://wise2.ipac.caltech.edu/docs/release/allsky/faq.html>.

Noll et al. 2009). Below we provide a detailed description of our SED fitting procedure in terms of the models and input priors, and present our fitting results.

4.1. Models

For galaxy SED fitting, in general, CIGALE requires four models in total, which describe the star-formation history (SFH), stellar populations, dust emission, and dust extinction, respectively. We do not use CIGALE’s default nebular emission model, as our sources do not exhibit strong nebular emission lines.

For SFH, we use two types of models: one or two exponentially declining recent bursts, with a main stellar population formed earlier (French et al. 2018a). We refer to these two kinds of models as ‘single-burst’ or ‘double-burst’ models hereafter. The common free parameters in both models are:

- (1) e -folding time of the main stellar population, τ_{main} ;
- (2) e -folding time of the most recent starburst population, τ_{burst} ;
- (3) mass fraction of the recent burst(s) relative to the total stellar mass, f_{burst} ;
- (4) age of the main stellar population (the time elapsed since it formed), age_{main} ;
- (5) age of the most recent burst (the time elapsed since it started), $\text{age}_{\text{burst}}$.

An additional free parameter, t_{sep} , is set in the double-burst model. It describes the time separation between the two recent bursts.

For stellar populations, we incorporate the BC03 (Bruzual & Charlot 2003) model assuming a Chabrier (2003) initial mass function (IMF). For dust emission, we choose the DL07 (Draine & Li 2007) model. For dust extinction, we use the Calzetti et al. (2000) law to model the internal extinction of our sources.

4.2. Input Priors

All of the input priors are summarized in Table 1. The prior values given are the allowed discrete values for CIGALE. For SFH, we refer to French et al. (2018a) for the number of recent bursts inferred for each galaxy. We give fairly large prior ranges for f_{burst} , $\text{age}_{\text{burst}}$, τ_{main} , τ_{burst} , age_{main} , and t_{sep} to enlarge the parameter space.

For the BC03 model, we offer a range of three metallicities closest to that inferred from the mass-metallicity relation for each object. The stellar masses come from the SDSS MPA-JHU catalogs (Brinchmann et al. 2004; Tremonti et al. 2004). The mass-metallicity relation is from Gallazzi et al. (2005).

For the DL07 model, the mass fraction of PAH, q_{PAH} , is allowed to vary from 0.47 to 4.58. The discrete values in Table 1 come directly from Draine & Li (2007). The prior range of the minimum radiation field (U_{min}) is set to [0.1, 25.0]. The fraction illuminated from U_{min} to U_{max} (γ) is

allowed to vary between [0.0001, 0.1]. We fix the maximum radiation field (U_{max}) to be 10^6 .

For the dust extinction model, we follow the default setting in CIGALE, which assumes that the stars younger than 10 Myr are subject to more extinction than the stars older than 10 Myr. We allow the color excess of the stellar continuum light for the young population, $E(B-V)_{\text{young}}$, to vary from 0.01 to 2. As the majority of our sample have $E(B-V)_{\text{young}} > 0.1$, we input six evenly distributed prior values from 0.1 to 2, and two values from 0.01 to 0.05. The reduction factor for the color excess of the old population compared to the young one, f_{att} , is allowed to vary from 0.3 to 1. We do not add any UV bump or power law to the original Calzetti et al. (2000) law.

4.3. Fitting Results

In Figure 1, we present eight typical SED fits of our sample. Their M_{dust} ’s range from $10^{5.78} M_{\odot}$ to $10^{8.18} M_{\odot}$, while the full range of M_{dust} of our sample is $10^{5.32} M_{\odot}$ to $10^{8.89} M_{\odot}$. According to French et al. (2018a), the optimal choice of a recent SFH model for EAH14, R3, A6, and F35 is ‘‘single-burst’’, whereas for EAH18, EAH9, R7, and A8 it is ‘‘double-burst’’.

To quantify the quality of our SED fits, we calculate the mean relative residual flux for our sample, as shown in Figure 2. We define the relative residual flux to be $(f_{\text{obs}} - f_{\text{model}})/f_{\text{obs}}$, in which f_{obs} is the observed flux and f_{model} is the model flux predicted by CIGALE. To determine the uncertainty of the mean relative residual flux, we use the Monte Carlo method to generate realizations of the fluxes and construct probability distributions for each individual flux and the mean relative residual flux. The error bars of the mean relative residual flux in Figure 2 represent their 68% confidence level uncertainties.

From Figure 2 we conclude that in general (i.e., for 19/20 bands), the mean relative residual flux is consistent with the 3σ average percentage flux uncertainty (defined as $\sigma_{\text{obs}}/f_{\text{obs}}$, where σ_{obs} is the total flux uncertainty in that band). For the W1 band, the mean relative residual flux is barely consistent with the 3σ average percentage flux uncertainty. Such systematics could be due to the uncertainties in the data, the limitations of the stellar population model, or the dust model.

In terms of reduced χ^2 , of all 58 SED fits, only five of the PSBs (EAH02, EAH05, EAH08, A5, and F35) have reduced $\chi^2 > 5.0$. Our tests show that their M_{dust} does not change much if we only fit their IR SED (see Appendix B). All five EAH sources with reduced $\chi^2 > 3.0$ have M_{dust} consistent with Smercina et al. (2018) (see Appendix C). So we conclude that the relatively large reduced χ^2 of this small fraction of our sample does not affect the robustness of our derived M_{dust} or any conclusions in general.

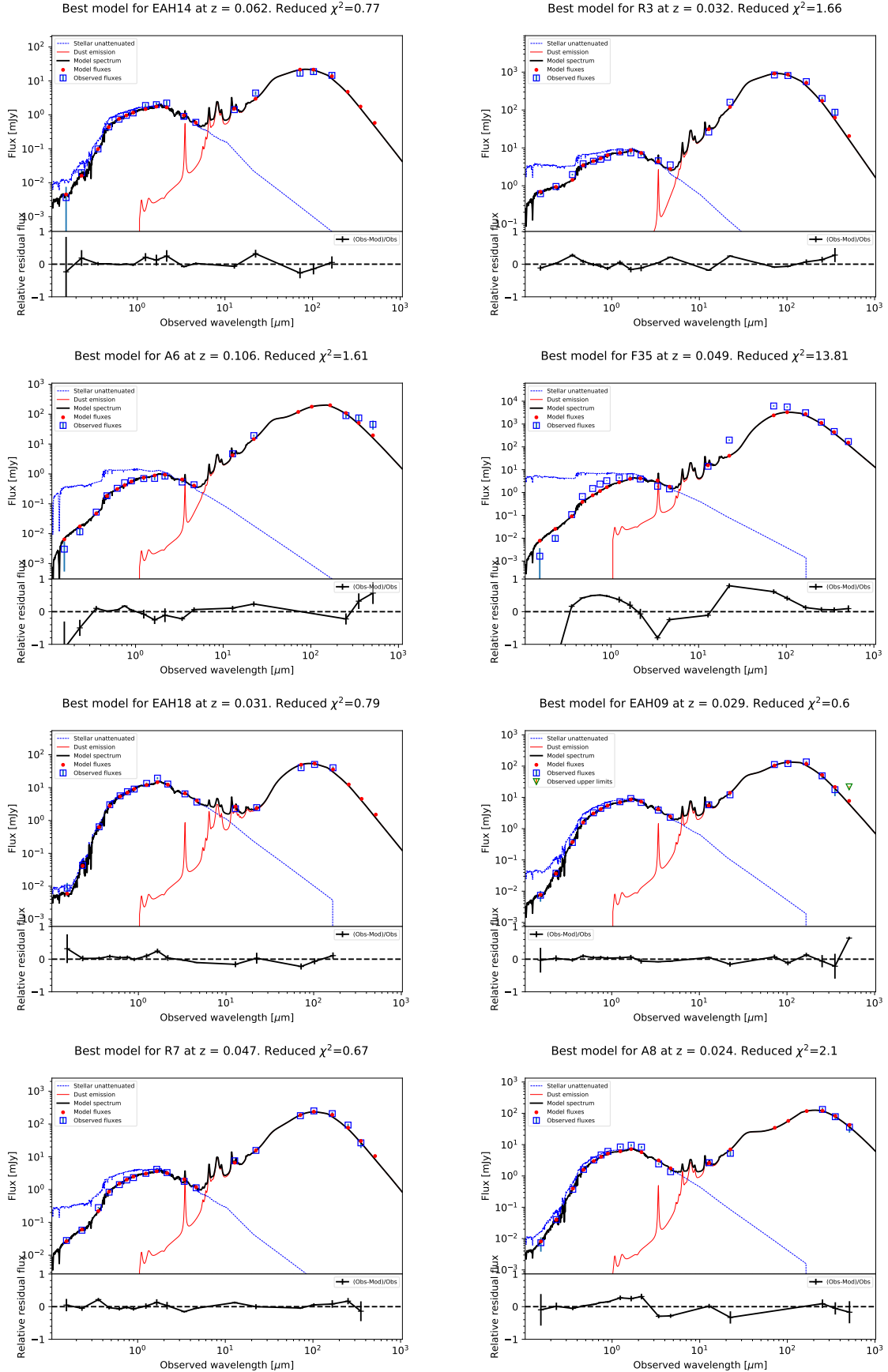


Figure 1. Eight representative SED fits derived from CIGALE. The top four fits have ‘single-burst’ SFH, whereas the bottom four have ‘double-burst’ SFH. The relative residual flux is defined as $(f_{\text{obs}} - f_{\text{model}})/f_{\text{obs}}$. The error bars (plotted in blue) are 1σ values. The green triangles represent 5σ upper limits. The worst fit here, F35, is particularly extended ($r_{50} = 7$ arcsec) and dusty.

Table 1. Input Parameters for CIGALE SED Fitting

Model	Parameter	Symbol	Prior Values
(1)	(2)	(3)	(4)
SFH	e -folding time of the main stellar population	τ_{main}	1.0, 2.0, 3.0 Gyr
	e -folding time of the recent burst	τ_{burst}	single-burst: 25, 50, 100, 200, 500 Myr double-burst: 25 Myr
	Mass fraction of the recent burst(s)	f_{burst}	0.01, 0.05, 0.1, 0.3, 0.5, 0.7, 0.9
	Age of the main stellar population	age_{main}	6.0, 9.0, 11.0 Gyr
	Age of the most recent burst	$\text{age}_{\text{burst}}$	30, 100, 200, 500, 1000, 1500, 2000 Myr
	Separation between two recent bursts	t_{sep}	double-burst: 100, 300, 500, 800, 1000 Myr
BC03	Metallicity	[Fe/H]	3 values inferred from Gallazzi et al. (2005)
DL07	Mass fraction of PAH	q_{PAH}	0.47, 1.12, 1.77, 2.50, 3.19, 4.58
	Minimum radiation field	U_{min}	0.10, 0.50, 1.00, 2.50, 5.0, 10.0, 25.0
	Maximum radiation field	U_{max}	10^6
	Dust fraction illuminated from U_{min} to U_{max}	γ	0.0001, 0.001, 0.01, 0.05, 0.1
	Power-law slope $dU/dM \propto U^\alpha$	α	2.0
Dust extinction	Color excess of stellar continuum light for young stars	$E(B - V)_{\text{young}}$	0.01, 0.05, 0.1, 0.4, 0.7, 1, 1.5, 2.0
	Reduction factor for $E(B - V)$ of old stars to young stars	f_{att}	0.3, 0.5, 0.8, 1.0

Note. Configurations of the input parameters used in CIGALE. (1) Model names. (2) Definitions of parameters. (3) Symbols of parameters. (4) Prior values of parameters.

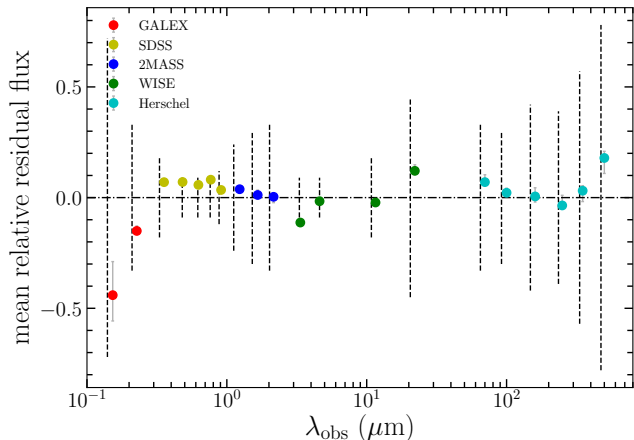


Figure 2. Mean relative residual flux (defined as $(f_{\text{obs}} - f_{\text{model}})/f_{\text{obs}}$) in different bands (marked in different colors) and its 68% confidence uncertainty after fitting the SEDs using CIGALE (Noll et al. 2009). For comparison, the vertical dashed lines are the 3σ average percentage flux uncertainty, defined as $\sigma_{\text{obs}}/f_{\text{obs}}$, where σ_{obs} is the total flux uncertainty in that band. The horizontal dotted-dashed line represents zero residual flux. In general (19/20 bands), the mean relative residual flux is consistent with the 3σ average percentage flux uncertainty, especially for all *Herschel* bands, which are crucial for deriving M_{dust} .

5. RESULTS AND DISCUSSION

5.1. M_{dust} versus post-burst age

Having derived M_{dust} for our sample using CIGALE, we examine the evolution of specific dust mass ($=M_{\text{dust}}/M_{\star}$) versus post-burst age, $\text{age}_{\text{post-burst}}$ ⁹. Here we define the ‘post-burst age’ to be the time elapsed since the majority (90%) of the stars formed in the recent burst(s). Thus, for the single-burst model, we have:

$$\text{age}_{\text{post-burst}} = \text{age}_{\text{burst}} - 2.3\tau_{\text{burst}} \quad (1)$$

while for the double-burst model¹⁰:

$$\text{age}_{\text{post-burst}} = \text{age}_{\text{burst}} - t_{\text{sep}} - 29 \quad (2)$$

As shown in Figure 3, there is a declining trend between specific dust mass and $\text{age}_{\text{post-burst}}$. To quantify the significance of this relation, we perform a Spearman rank test and linear fitting using the method in Cappellari et al. (2013), which takes errors in both $M_{\text{dust}}/M_{\star}$ and $\text{age}_{\text{post-burst}}$ into account. The fitting result is in the form of $\log(M_{\text{dust}}/M_{\star}) = a \cdot (\text{age}_{\text{post-burst}} - x_0) + b + \epsilon$, where $a = -0.00212 \pm 0.00047$, $b = -3.28 \pm 0.10$, $x_0 = 316$, and intrinsic scatter $\epsilon = 0.68 \pm 0.09$. We also use the ASURV survival analysis

⁹ We use the more accurate $\text{age}_{\text{post-burst}}$ derived in French et al. (2018a) by including optical spectral information (see Appendix D).

¹⁰ Here τ_{burst} is fixed to 25 Myr.

package to calculate the Spearman’s rank correlation (Isobe et al. 1986; Lavalley et al. 1992), and perform bootstrap analysis (1000 samples) to derive the confidence intervals of the Spearman correlation coefficient and the null hypothesis probability (Lanz et al. 2019). The null hypothesis is that there is no monotonic relation between two parameters. We define a significant correlation as one that rejects this hypothesis by having a probability $\leq 3 \times 10^{-3}$ ($\log(p) \leq -2.52$), corresponding to approximately 3σ . The Spearman coefficients are $r = -0.39 \pm 0.13$ and $\log(p) = -2.54 \pm 1.24$. To compare our results with previous work, we overplot three other samples following Rowlands et al. (2015). They are the average $M_{\text{dust}}/M_{\star}$ for $z < 0.1$ spiral galaxies detected in Rowlands et al. (2012), for $0.01 < z < 0.06$ dusty ETGs from Agius et al. (2013), and for nondusty ETGs (representative of red sequence galaxies) for a range of dust temperatures from Rowlands et al. (2012).

The significant anti-correlation between $M_{\text{dust}}/M_{\star}$ and $\text{age}_{\text{post-burst}}$ suggests that the dust is either destroyed, expelled, or rendered undetectable over the ~ 1 Gyr after the burst. Assuming the $M_{\text{dust}}/M_{\star}$ depletes exponentially after the burst ends, the fitting yields a depletion timescale of 205^{+58}_{-37} Myr. Such a timescale is consistent with the M_{H_2}/M_{\star} depletion timescale (117-230 Myr) derived in French et al. (2018a). Considering the typical $M_{\text{dust}}/M_{\star}$ of our sample at zero $\text{age}_{\text{post-burst}}$ (~ -2.5) and the $M_{\text{dust}}/M_{\star}$ range of non-dusty ETGs, it should take ~ 1 -2 Gyr for PSBs reach early-type levels of $M_{\text{dust}}/M_{\star}$. This result is consistent with previous claims that PSB stellar populations, color gradients, morphologies, kinematics, and molecular gas (Norton et al. 2001; Yang et al. 2004, 2008; Pracy et al. 2013; Pawlik et al. 2016; French et al. 2018a) will resemble the properties of ETGs in a few Gyr.

The derived $M_{\text{dust}}/M_{\star}$ depletion timescale may be, at least partly, due to the low-ionization nuclear emission-line region (LINER) or active galactic nucleus (AGN) feedback, as gas consumption by residual star formation would take much longer time (French et al. 2018a). The depletion time associated with AGN driven outflows in non-AGN-dominated starburst galaxies could be up to several hundred Myr (Cicone et al. 2014; Baron et al. 2017, 2018), which is consistent with our case here.

We do not find any significant correlation between $M_{\text{H}_2}/M_{\text{dust}}$ and $\text{age}_{\text{post-burst}}$ (Spearman coefficients $r = 0.11 \pm 0.16$, $\log(p) = -0.33 \pm 0.54$). The decrease in $M_{\text{dust}}/M_{\star}$ and M_{H_2}/M_{\star} with $\text{age}_{\text{post-burst}}$ and the constancy of the gas-to-dust ratio suggest that the dust and gas decline is driven by the same physical mechanism. Furthermore, the close mutual tracking of the gas and dust indicates that the mechanism removes, consumes, or expels the ISM material, instead of merely altering its state and rendering it undetectable.

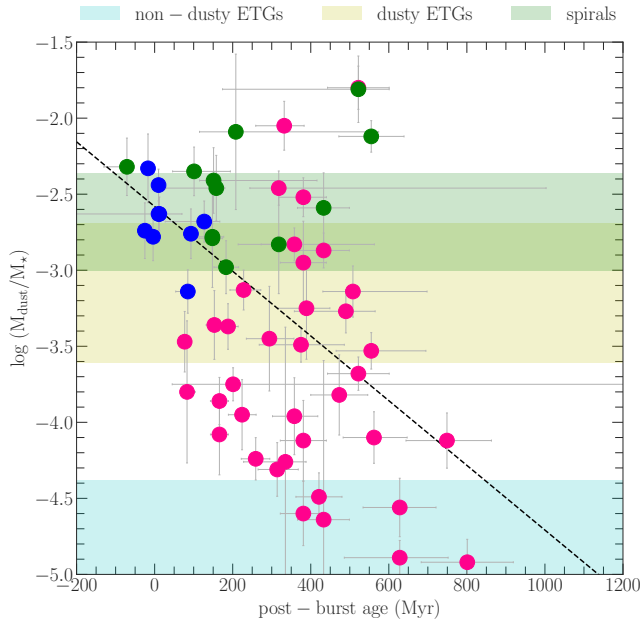


Figure 3. Specific dust mass (M_{dust}/M_*) vs. post-burst age relation. The green points represent the 12 PSBs from Alatalo et al. (2016a), the red points are the 37 PSBs from French et al. (2018a), and the blue points are the nine PSBs from Rowlands et al. (2015). The black dotted line is a linear fit using the method in Cappellari et al. (2013): $\log(M_{\text{dust}}/M_*) = a \cdot (\text{age}_{\text{post-burst}} - x_0) + b + \epsilon$, where $a = -0.00212 \pm 0.00047$, $b = -3.28 \pm 0.10$, $x_0 = 316$, and the intrinsic scatter $\epsilon = 0.68 \pm 0.09$. The Spearman coefficients are $r = -0.39 \pm 0.13$ and $\log(p) = -2.54 \pm 1.24$. To compare our results with previous work, we overplot three other samples following Rowlands et al. (2015): the average M_{dust}/M_* for $z < 0.1$ spiral galaxies in Rowlands et al. (2012), $0.01 < z < 0.06$ dusty ETGs from Agius et al. (2013), and nondusty ETGs for a range of dust temperatures from Rowlands et al. (2012). The significant declining trend between M_{dust}/M_* and $\text{age}_{\text{post-burst}}$ implies a dust depletion timescale of 205_{-37}^{+58} Myr, consistent with the CO-traced H_2 depletion timescale (French et al. 2018a).

5.2. M_{dust} versus SFR and M_{H_2}

Molecular gas, interstellar dust, and star formation are strongly correlated with each other in galaxies. The dust grains produced in supernovae can protect molecular hydrogen from UV radiation and contribute to the formation of molecular clouds, which collapse to form new stars. To quantify these relationships in PSBs, we consider here the relations between M_{dust} and SFR and between M_{dust} and molecular gas mass, M_{H_2} . The latter relation is a useful calibration to convert M_{dust} into harder-to-measure M_{H_2} .

To consider the SFR- M_{dust} relation for our sample, we convert the $\text{H}\alpha$ fluxes from the MPA-JHU catalog (Aihara et al. 2011) to SFR using the relation from Kennicutt et al.

(1994)¹¹. We estimate the amount of internal dust extinction from the observed Balmer decrement, $\text{H}\alpha/\text{H}\beta$. Assuming the hydrogen nebular emission follows Case B recombination, the intrinsic Balmer flux ratio $(\text{H}\alpha/\text{H}\beta)_0 = 2.86$ for $T_e = 10^4$ K. Following French et al. (2015), we adopt the reddening curve of O'Donnell (1994)¹². When the $\text{H}\beta$ line flux is uncertain, we follow French et al. (2015) using the mean value of $E(B-V)$ of the other PSBs in French et al. (2015). The mean attenuation is $A_V = 0.92$ mag (or $A_{\text{H}\alpha} = 0.77$ mag).

We further correct for potential underlying AGN contribution to $\text{H}\alpha$ fluxes following the methodology from Wild et al. (2010). We calculate the emission-line ratios $[\text{O III}]\lambda 5007/\text{H}\beta$ and $[\text{N II}]\lambda 6583/\text{H}\alpha$ of our PSBs to pinpoint them on the BPT diagram (Baldwin et al. 1981; Veilleux & Osterbrock 1987), and determine the AGN contribution to their $\text{H}\alpha$ luminosities. In some cases, a negative SFR correction factor is derived, of which the corresponding 1σ upper limit is positive. We designate the SFR in these cases to be 1σ upper limit values. In addition, when the $\text{H}\beta$ line is not well detected, we use its uncertainty as the 1σ flux upper limit to determine the corresponding 1σ upper limit for the correction factor. Note that all the SFR 1σ upper limits are due to AGN correction, instead of low S/N $\text{H}\alpha$ detections. In fact, all of our PSBs have $\geq 9\sigma$ $\text{H}\alpha$ detections, except for two 5σ detections (EAS07 and EAS08) and two 4σ detections (EAS10 and EAH10). All the SFR values are provided in Table 4.

Our results are shown in Figure 4. For comparison, we plot the lines fit to 1658 local star-forming galaxies from da Cunha et al. (2010) and to 843 $z < 0.5$ H-ATLAS star-forming galaxies from Rowlands et al. (2014). At fixed M_{dust} , our PSBs tend to have lower SFR than the local star-forming galaxies. This reflects the nature of PSBs, which have low SFRs by definition. The Spearman coefficients for the PSB $\log \text{SFR} - \log M_{\text{dust}}$ relation are $r = 0.56 \pm 0.12$ and $\log(p) = -3.70 \pm 1.34$, indicating a significant correlation. Even for the French et al. (2018a) sample alone, PSBs with the lowest M_{dust} generally have the lowest SFRs.

Next we fit the relationship between M_{dust} and M_{H_2} for those 44 PSBs with both dust and CO measurements (the latter from French et al. 2015, Rowlands et al. 2015, and Alatalo et al. 2016b). We adopt the linear regression method from Kelly (2007), which takes both detections and upper limits into account. The best-fitting result is in the form of $\log M_{\text{H}_2} = a \cdot \log M_{\text{dust}} + b + \epsilon$, where $a = 0.45 \pm 0.10$, $b =$

¹¹ We do not use IR-derived SFRs in this paper, because (1) they are prone to overestimation (Hayward et al. 2014; Smercina et al. 2018), and (2) we want to avoid the intrinsic correlation between IR-derived M_{dust} and IR-derived SFRs.

¹² Using Calzetti et al. (2000) would yield a negligible difference: $A_{\text{H}\alpha}/A_V = 0.82$ instead of 0.84, assuming $R_V = 4.05$.

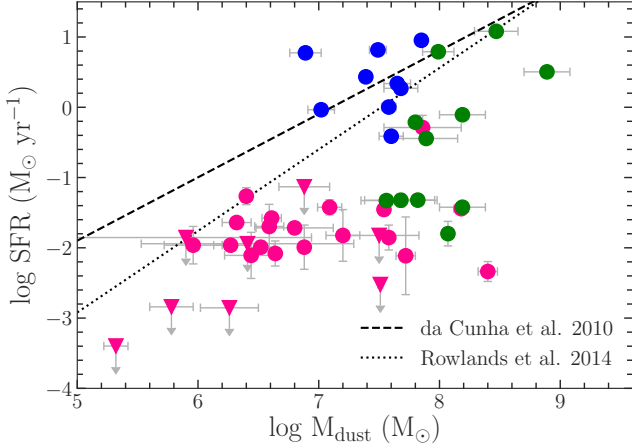


Figure 4. Star formation rate (SFR) vs. dust mass (M_{dust}) relation. The data points are colored as in Figure 3. The Spearman coefficients are $r = 0.56 \pm 0.12$ and $\log(p) = -3.70 \pm 1.34$, indicating a significant correlation. The black dashed line is derived by fitting 1658 local star-forming galaxies from da Cunha et al. (2010). The black dotted line is a fit to 843 $z < 0.5$ H-ATLAS star-forming galaxies from Rowlands et al. (2014). The triangles pointing downwards are objects with SFR 1σ upper limits. Even only within the French et al. (2018a) sample (red points), PSBs with the lowest M_{dust} tend to have the lowest SFRs.

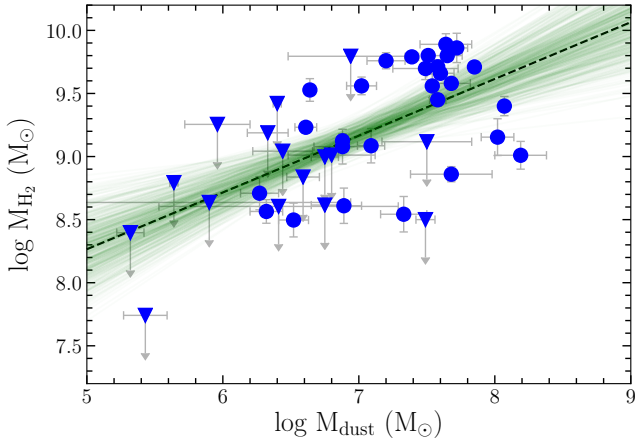


Figure 5. The $M_{\text{dust}}-M_{\text{H}_2}$ relation for our 44 PSBs with CO detections (blue solid circles) and 3σ upper limits (blue solid triangles). The black dashed line is the best fit to the relation $\log M_{\text{H}_2} = a \cdot \log M_{\text{dust}} + b + \epsilon$, where $a = 0.45 \pm 0.10$, $b = 6.02 \pm 0.68$, and the intrinsic scatter $\epsilon = 0.42 \pm 0.05$, derived via linear regression (Kelly 2007). The green lines represent 500 evenly spaced samples from the posterior distribution of the model parameters. There is a tight correlation between M_{dust} and M_{H_2} , with Spearman coefficients $r = 0.69 \pm 0.08$ and $\log(p) = -5.15 \pm 1.03$, which is then useful in estimating M_{H_2} from easier-to-measure M_{dust} .

6.02 ± 0.68 , and intrinsic scatter $\epsilon = 0.42 \pm 0.05$ (see Figure 5). The Spearman coefficients are $r = 0.69 \pm 0.08$ and $\log(p) = -5.15 \pm 1.03$. We use this significant correlation between M_{dust} and M_{H_2} as a calibration, applying it to those 14 PSBs without molecular gas measurements to derive their M_{H_2} .

5.3. Kennicutt-Schmidt relation

The relationships among SFR, M_{dust} , and M_{H_2} for PSBs motivate us to explore the KS relation¹³. With our $M_{\text{dust}}-M_{\text{H}_2}$ calibration, we deduce M_{H_2} for those PSBs without CO detections, and use the SDSS Petrosian radius¹⁴ (r_{50}) to convert M_{dust} , M_{H_2} , and SFR into surface mass densities. The resulting $\Sigma\text{SFR}-\Sigma M_{\text{dust}}$ and $\Sigma\text{SFR}-\Sigma M_{\text{H}_2}$ relations are in Figure 6.

Next we compare our 33 PSBs that have SFR detections and M_{H_2} measurements from either CO emission or the $M_{\text{dust}}-M_{\text{H}_2}$ calibration with normal star-forming galaxies and starbursts from Kennicutt (1998) and with ETGs from Davis et al. (2014). For the ETG sample, we recalculate ΣSFR and ΣM_{H_2} using r_{50} to ensure a direct comparison to the PSB sample. For the Kennicutt (1998) sample, we use the original surface densities normalized by the RC2 isophotal radius (where the B -band surface brightness drops to 25 mag arcmin⁻²), which is comparable to the H α emitting region for normal spiral galaxies, as the r_{50} is unavailable in the SDSS. French et al. (2015) explored the effects of assuming different radii and found consistent results.

Figure 7 shows that the locus of our PSBs lies below the KS relation for the other galaxies (as was seen by French et al. 2015). Scaling the surface densities of these galaxies with a different radius would move them along the KS relation, which does not eliminate the observed offset for our PSBs. Remarkably, when we consider their post-burst ages, the PSBs evolve downward during the first 200-300 Myr, due to the faster decrease in ΣSFR relative to ΣM_{H_2} . This evolution also implies a decreasing SFE, defined here as $\Sigma\text{SFR}/\Sigma M_{\text{H}_2}$ (or $\text{SFR}/M_{\text{H}_2}$). The SFE later reaches and remains at a low value, $\sim 10^{-11} \text{ yr}^{-1}$, ≥ 300 Myr after the burst.

5.4. Star formation efficiency

¹³ The version of the KS relation (Kennicutt 1998) for SFR and M_{H_2} in local normal disk galaxies is $\Sigma\text{SFR} \propto \Sigma M_{\text{H}_2}^{1.0}$ (Leroy et al. 2013), where the exact slope is sensitive to the tracer (e.g., Gao & Solomon 2004) and the CO-to- H_2 conversion factor (e.g., Bolatto et al. 2013).

¹⁴ Without resolved IR, CO, and H α observations for all of our sample, we assume that the dust, molecular gas, and star formation regions are roughly comparable in size and lie within r_{50} . We do know that, for a subsample of these galaxies, the dust typically subtends a radius 3-4 \times smaller than r_{50} (Smercina et al. 2018) and that, for four (EAS02, 04, 11, 13), the H α emission does not extend much beyond r_{50} in archival MaNGA (Bundy et al. 2015) data.

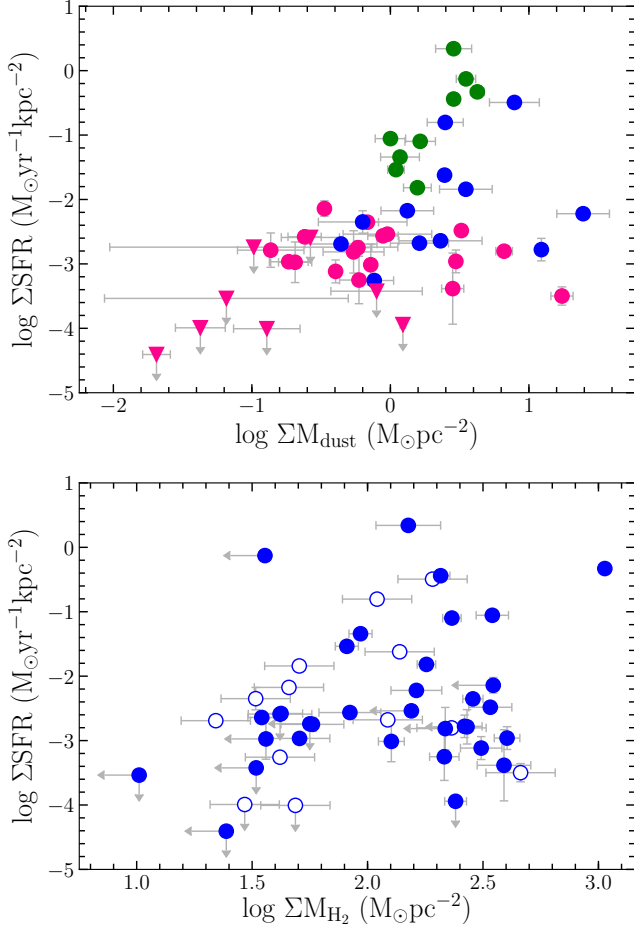


Figure 6. The $\Sigma\text{SFR}-\Sigma M_{\text{dust}}$ and $\Sigma\text{SFR}-\Sigma M_{\text{H}_2}$ planes for our PSBs. Upper: the points are color-coded as in Figure 3. 1σ upper limits are marked with y-axis arrows. Lower: all the PSBs with CO detections or 3σ upper limits (x-axis arrows) from Figure 5 are marked with filled circles, and the PSBs with M_{H_2} deduced from the $M_{\text{dust}}-M_{\text{H}_2}$ calibration are open circles. Only those PSBs with SFR detections or 1σ upper limits (y-axis arrows) are shown. The Spearman coefficients are $r = 0.54 \pm 0.12$, $\log(p) = -3.52 \pm 1.26$ for the $\Sigma\text{SFR}-\Sigma M_{\text{dust}}$ relation, and $r = 0.11 \pm 0.17$, $\log(p) = -0.34 \pm 0.59$ for the $\Sigma\text{SFR}-\Sigma M_{\text{H}_2}$ relation.

The evolution of SFE for our PSB sample is shown directly in Figure 8. SFE drops significantly with post-burst age. After the first ~ 200 -300 Myr, the SFE decline slows¹⁵. To ultimately reach the SFE level of ETGs, there must be an increase in SFE later.

The fast initial SFE decline arises from SFR decreasing more quickly than M_{H_2} . The decoupling of SFR from M_{H_2} suggested by this result is consistent with French et al. (2018a), who found that the decline of M_{H_2}/M_* is too quick

to arise from consumption by star formation and is similar to the observed outflow rates of AGN/LINERS. Such outflows may not only drive the M_{H_2}/M_* decline, but also prevent the large CO-traced molecular gas reservoirs from collapsing and forming denser, star-forming clouds. The rapid drop in SFR is in fact likely due to the absence of denser gas (as traced by HCO^+/HCN ; French et al. 2018b). Any successful feedback model will need to reproduce these behaviors, namely that M_{H_2}/M_* and M_{dust}/M_* decline similarly over a timescale of several hundred Myr and that denser gas and SFR decline faster than M_{H_2} and M_{dust} .

The slowing of the SFR decline, after the first ~ 200 -300 Myr, was also seen in Figure 7. If we assume that the SFR's value at ~ 500 Myr remains constant thereafter, and that the depletion of M_{H_2} continues (French et al. 2018a), then the SFE will rise to ETG levels within ~ 0.5 -1.1 Gyr (or equivalently, ~ 1 -1.6 Gyr after the most recent burst ends).

6. CONCLUSIONS

By performing UV-FIR SED fitting for a sample of 58 PSBs, we have determined M_{dust} and quantified the relationship between M_{dust} and CO-traced M_{H_2} . We have also observed evolution with post-burst age in M_{dust}/M_* , SFE, and the KS plane. Our main results are:

(1) There is a significant anticorrelation between the M_{dust}/M_* and the time elapsed since the end of the recent starburst ($\text{age}_{\text{post-burst}}$), indicating that the dust is either destroyed, expelled, or rendered undetectable over the ~ 1 Gyr after the burst. Assuming that the M_{dust}/M_* depletes exponentially after the burst ends yields a depletion timescale of 205^{+58}_{-37} Myr. This timescale is consistent with the CO-traced M_{H_2}/M_* depletion timescale (French et al. 2018a), suggesting that these dust and molecular gas evolution trends are real and due to the same mechanism. Intriguingly, this observed decline will reduce the dust and CO reservoirs of a PSB to that of an ETG within 1-2 Gyr, when the PSB stellar populations, color gradients, morphologies, and kinematics will likewise resemble those of ETGs.

(2) We determine the $M_{\text{dust}}-M_{\text{H}_2}$ relation from our 44 PSBs with both M_{dust} and CO detections, and apply this calibration to estimate M_{H_2} for the remainder of the sample. We then place the PSBs in the KS plane and find that over time, they move down and away from the KS relation defined by normal star-forming galaxies and starbursts. This evolution is principally due to a rapid drop in the SFR, at least for the first 200-300 Myr after the burst ends.

(3) Direct examination of the evolution of SFE (the ratio of SFR to the CO-traced M_{H_2}) reveals a sharp drop during those first 200-300 Myr, i.e., the SFR is decoupled from the M_{H_2} and declines faster. The decrease in SFR in PSBs is likely due to the absence of denser gas (French et al. 2018b). It is possible that the same mechanism responsible for the decline

¹⁵ The apparent SFE floor is not due to a limit in our SFR measurement sensitivity: across the ranges of SFEs and post-burst ages plotted here, the S/N of the $\text{H}\alpha$ detections is similar and high (see section 5.2).

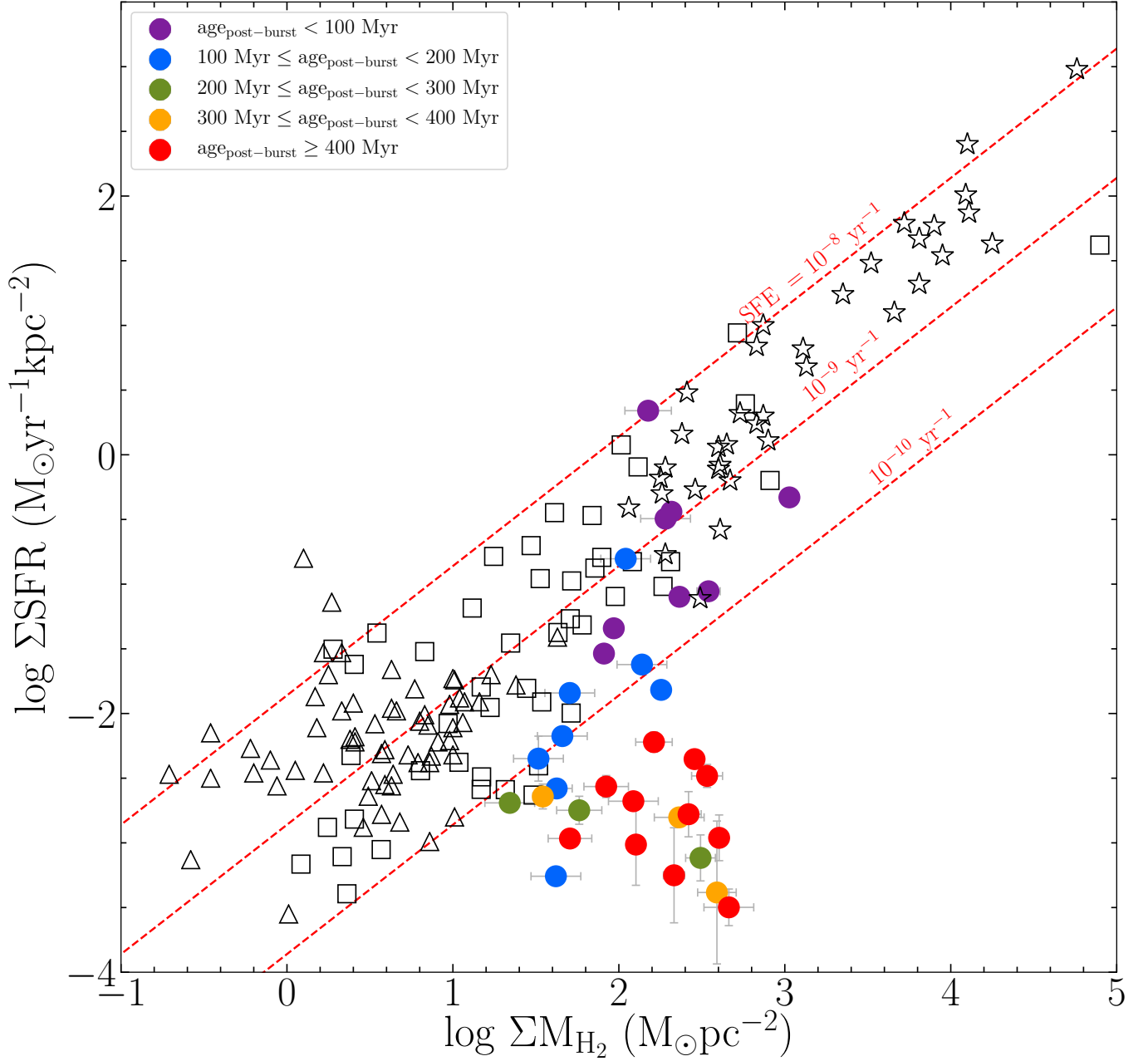


Figure 7. Time evolution of PSBs in the Kennicutt-Schmidt plane (the x -axis here is defined as in Leroy et al. 2013). The locus of the PSB sample (filled circles) lies below the KS relation for other galaxies (see French et al. 2015). Normal star forming (open, black triangles) and starburst (stars) galaxies are from Kennicutt (1998). ETGs (open squares) are from Davis et al. (2014). Our PSB sample is binned by increasing post-burst ages, from purple to red. To be conservative, we include only detections, not the upper limits from Figure 6. The PSBs evolve down off the relation over time, due to the faster decrease in ΣSFR relative to ΣM_{H_2} , especially during the first 200–300 Myr. This evolution implies a changing SFE. We show three different, constant SFEs (red, dashed lines): the consumption of 1%, 10%, and 100% of the gas reservoir by star formation per 10^8 yr, or, equivalently, 10^{-10} – 10^{-8} yr^{-1} . Later, ~ 300 Myr after the burst, the SFE reaches and remains at a low value, $\sim 10^{-11}$ yr^{-1} .

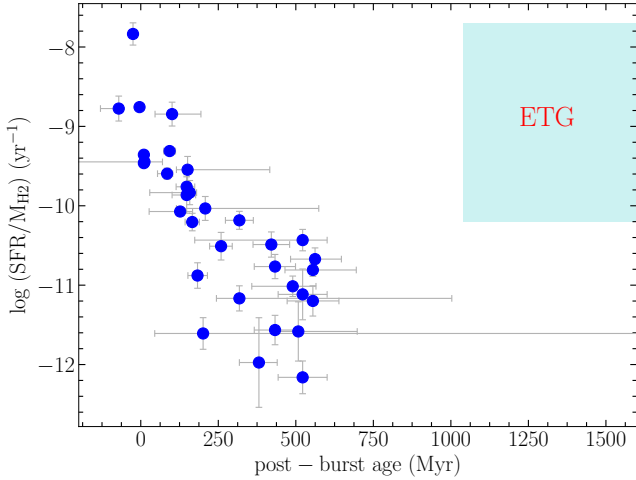


Figure 8. Time evolution of the PSB star formation efficiency. Galaxies are the same as in Figure 7. There is a significant initial decline in SFE with post-burst age; the Spearman coefficients are $r = -0.88 \pm 0.07$, $\log(p) = -3.70 \pm 0.52$ for PSBs with $\text{age}_{\text{post-burst}} < 300$ Myr. After ~ 200 -300 Myr, the SFE decrease slows, reaching an apparent floor of $\sim 10^{-11} \text{ yr}^{-1}$. If we assume that the SFR reaches a constant value after ~ 500 Myr, and that the depletion rate of M_{H_2} does not change, the SFE of PSBs would rise to ETG levels (cyan region; Davis et al. 2014) in another ~ 0.5 -1.1 Gyr (or ~ 1 -1.6 Gyr after the recent burst ends). This timescale is consistent with the evolution of other PSB properties into ETGs.

in M_{H_2}/M_* and M_{dust}/M_* , whose common short timescale is consistent with AGN/LINER feedback, also prevents the large CO-traced molecular gas reservoirs from collapsing and forming denser, star-forming clouds. After ~ 200 -300 Myr, the M_{H_2} continues to decline, but the SFR levels off, suggesting an SFE floor of 10^{-11} yr^{-1} . If we assume that the SFR remains constant at this late level, and that the depletion rate of M_{H_2} does not change, then the SFE will rise to ETG levels within ~ 0.5 -1.1 Gyr, a timescale consistent with the evolution of other PSB properties into ETGs.

We are grateful to the anonymous referee for carefully reading our manuscript and providing constructive feedback, which substantially helped improving the quality of this paper. We thank Adam Smercina, Daniel A. Dale, and Dennis Zaritsky for constructive suggestions and helpful discussions. We also thank Yuguang Chen and Michael Zhang for help in installing the `asurv` package and debugging. Z.L. is grateful for support from the Study Abroad Scholarship for Excellent Students by China Scholarship Council for undergraduate research. K.D.F. is supported by program HST-HF2-51391.001-A, provided by NASA through a grant from the Space Telescope Science Institute, which is operated by the Association of Universities for Research in Astronomy, Incorporated, under NASA contract NAS5-26555. A.I.Z. acknowledges funding from NASA grant

ADP-NNX10AE88G. L.C.H. was supported by the National Key R&D Program of China (2016YFA0400702) and the National Science Foundation of China (11721303).

This work has made use of the data obtained by *GALEX*, SDSS, 2MASS, *WISE* and *Herschel*. Funding for the Sloan Digital Sky Survey IV has been provided by the Alfred P. Sloan Foundation, the U.S. Department of Energy Office of Science, and the Participating Institutions. SDSS-IV acknowledges support and resources from the Center for High-Performance Computing at the University of Utah. The SDSS website is <http://www.sdss.org/>. SDSS-IV is managed by the Astrophysical Research Consortium for the Participating Institutions of the SDSS Collaboration including the Brazilian Participation Group, the Carnegie Institution for Science, Carnegie Mellon University, the Chilean Participation Group, the French Participation Group, Harvard-Smithsonian Center for Astrophysics, Instituto de Astrofísica de Canarias, The Johns Hopkins University, Kavli Institute for the Physics and Mathematics of the Universe (IPMU) / University of Tokyo, Lawrence Berkeley National Laboratory, Leibniz Institut für Astrophysik Potsdam (AIP), Max-Planck-Institut für Astronomie (MPIA Heidelberg), Max-Planck-Institut für Astrophysik (MPA Garching), Max-Planck-Institut für Extraterrestrische Physik (MPE), National Astronomical Observatories of China, New Mexico State University, New York University, University of Notre Dame, Observatório Nacional / MCTI, The Ohio State University, Pennsylvania State University, Shanghai Astronomical Observatory, United Kingdom Participation Group, Universidad Nacional Autónoma de México, University of Arizona, University of Colorado Boulder, University of Oxford, University of Portsmouth, University of Utah, University of Virginia, University of Washington, University of Wisconsin, Vanderbilt University, and Yale University. This publication makes use of data products from the Two Micron All-Sky Survey, which is a joint project of the University of Massachusetts and the Infrared Processing and Analysis Center/California Institute of Technology, funded by the National Aeronautics and Space Administration and the National Science Foundation. *WISE* is a joint project of the University of California, Los Angeles, and the Jet Propulsion Laboratory of California Institute of Technology, funded by the National Aeronautics and Space Administration. The *WISE* website is <http://wise.astro.ucla.edu/>. *Herschel* is an ESA space observatory with science instruments provided by European-led Principal Investigator consortia and with important participation from NASA.

Table 2 (continued)

ID	R.A.	Decl.	GALEX (mJy)		SDSS (mJy)					2MASS (mJy)		
	(J2000 deg)	(J2000 deg)	FUV	NUV	<i>u</i>	<i>g</i>	<i>r</i>	<i>i</i>	<i>z</i>	<i>J</i>	<i>H</i>	<i>Ks</i>
(1)	(2)	(3)	(4)	(5)	(6)	(7)	(8)	(9)	(10)	(11)	(12)	(13)

Note. (1) Object ID. R1-R11 are from Rowlands et al. (2015); EAH01-EAH18, EAS01-EAS15 and F34-F37 are from French et al. (2018a), and A1-A12 are from Alatalo et al. (2016a). (2)-(3) Right ascension and declination. (4)-(5) GALEX fluxes. (6)-(10) SDSS fluxes. (11)-(13) 2MASS fluxes. All fluxes are given in mJy. The total flux uncertainties, which correspond to 68% confidence levels, are given in parentheses when available. No correction for extinction has been applied.

Table 3. Archival MIR-FIR Photometry

ID	WISE (mJy)				Herschel-PACS (mJy)			Herschel-SPIRE (mJy)		
	W1(3.6 μ m)	W2(4.5 μ m)	W3(12 μ m)	W4(22 μ m)	70 μ m	100 μ m	160 μ m	250 μ m	350 μ m	500 μ m
(1)	(2)	(3)	(4)	(5)	(6)	(7)	(8)	(9)	(10)	(11)
R1	3.71E+00 (2.39E-02)	2.93E+00 (2.70E-02)	3.00E+01 (1.66E-01)	1.62E+02 (1.79E+00)	1.15E+03 (2.33E+01)	1.24E+03 (3.35E+01)	9.70E+02 (3.16E+01)	3.90E+02 (1.49E+01)	1.68E+02 (1.96E+01)	6.09E+01 (1.72E+01)
R2	7.79E+00 (4.30E-02)	6.23E+00 (4.01E-02)	5.35E+01 (2.95E-01)	2.30E+02 (1.48E+00)	3.58E+03 (5.64E+01)	3.76E+03 (8.14E+01)	2.58E+03 (6.16E+01)	9.10E+02 (1.94E+01)	3.21E+02 (1.65E+01)	1.05E+02 (1.88E+01)
R3	4.57E+00 (2.94E-02)	3.56E+00 (2.94E-02)	2.62E+01 (1.93E-01)	1.60E+02 (3.24E+00)	8.42E+02 (2.09E+01)	8.13E+02 (2.63E+01)	5.62E+02 (4.23E+01)	2.02E+02 (1.78E+01)	8.71E+01 (1.88E+01)	...
R4	6.61E+00 (3.65E-02)	4.66E+00 (3.00E-02)	3.54E+01 (1.95E-01)	8.19E+01 (9.79E-01)	1.52E+03 (3.41E+01)	1.96E+03 (4.79E+01)	2.01E+03 (5.62E+01)	8.16E+02 (1.59E+01)	3.48E+02 (1.86E+01)	1.31E+02 (1.93E+01)
R5	3.38E+00 (2.18E-02)	2.99E+00 (2.48E-02)	3.78E+01 (2.43E-01)	1.81E+02 (2.16E+00)	1.15E+03 (1.85E+01)	1.28E+03 (3.15E+01)	1.01E+03 (3.98E+01)	4.13E+02 (1.40E+01)	1.67E+02 (1.31E+01)	5.25E+01 (1.20E+01)
R6	3.40E+00 (1.88E-02)	2.18E+00 (1.60E-02)	1.05E+01 (8.72E-02)	2.76E+01 (9.41E-01)	4.11E+02 (1.22E+01)	5.46E+02 (1.79E+01)	6.01E+02 (2.90E+01)
R7	1.78E+00 (3.93E-02)	1.14E+00 (2.93E-02)	7.57E+00 (2.30E-01)	1.57E+01 (1.18E+00)	1.80E+02 (5.28E+00)	2.51E+02 (1.20E+01)	2.07E+02 (2.41E+01)	9.29E+01 (8.90E+00)	2.67E+01 (8.10E+00)	...
R9	1.39E+00 (8.96E-03)	8.31E-01 (9.94E-03)	3.29E+00 (3.63E-02)	5.25E+00 (4.49E-01)	1.49E+02 (7.44E+00)	2.58E+02 (1.28E+01)	3.10E+02 (1.80E+01)
R10	2.74E+00 (1.51E-02)	1.92E+00 (2.12E-02)	1.09E+01 (9.04E-02)	2.33E+01 (9.87E-01)	7.44E+02 (2.02E+01)	1.01E+03 (2.96E+01)	9.57E+02 (4.46E+01)	4.06E+02 (1.29E+01)	1.57E+02 (1.38E+01)	6.07E+01 (1.31E+01)
F34	1.03E+00 (6.64E-02)	6.20E-01 (4.20E-02)	1.30E+00 (1.72E-01)	4.05E+00 (1.22E+00)	...	3.33E+01 (1.11E+01)	5.93E+01 (1.06E+01)	4.21E+01 (9.85E+00)
F35	1.88E+00 (1.30E-01)	1.45E+00 (9.98E-02)	1.41E+01 (9.55E-01)	1.98E+02 (1.42E+01)	6.17E+03 (4.40E+02)	5.59E+03 (4.03E+02)	3.12E+03 (2.24E+02)	1.20E+03 (8.61E+01)	4.70E+02 (3.54E+01)	1.70E+02 (1.70E+01)
F36	1.34E+00 (8.61E-02)	8.88E-01 (5.90E-02)	3.57E+00 (2.68E-01)	1.34E+01 (1.52E+00)	9.37E+01 (6.01E+01)	6.09E+01 (1.56E+01)	5.03E+01 (1.52E+01)	...
F37	4.71E+00 (2.84E-01)	2.61E+00 (1.58E-01)	1.95E+00 (1.44E-01)	4.39E+00 (8.73E-01)	5.90E+01 (6.37E+00)	7.77E+01 (1.07E+01)	6.48E+01 (1.27E+01)
A1	4.02E-01 (2.66E-02)	3.34E-01 (2.50E-02)	1.95E+00 (1.83E-01)	7.02E+00 (1.19E+00)	...	7.48E+01 (1.33E+01)	8.46E+01 (2.77E+01)	4.84E+01 (1.52E+01)
A2	4.48E-01 (2.98E-02)	3.07E-01 (2.37E-02)	1.91E+00 (1.89E-01)	3.20E+00 (1.10E+00)	...	7.60E+01 (1.52E+01)	1.47E+02 (2.88E+01)	7.39E+01 (1.27E+01)
A3	9.19E-01 (5.91E-02)	7.44E-01 (4.83E-02)	2.18E+00 (1.82E-01)	6.41E+00 (1.07E+00)	1.31E+02 (1.35E+01)	5.86E+01 (1.15E+01)	3.41E+01 (7.68E+00)
A4	1.23E+00 (7.87E-02)	9.71E-01 (6.27E-02)	6.23E+00 (4.07E-01)	1.74E+01 (1.37E+00)	1.04E+02 (1.38E+01)	8.53E+01 (1.67E+01)	6.35E+01 (1.48E+01)
A5	1.70E+01 (1.02E+00)	1.03E+01 (6.23E-01)	4.16E+01 (2.51E+00)	5.78E+02 (3.48E+01)	1.97E+04 (1.41E+03)	1.81E+04 (1.31E+03)	1.05E+04 (7.55E+02)	4.15E+03 (2.94E+02)	1.69E+03 (1.21E+02)	5.90E+02 (4.77E+01)

Table 3 continued

Table 3 (continued)

ID	WISE (mJy)				Herschel-PACS (mJy)			Herschel-SPIRE (mJy)		
	W1(3.6 μ m)	W2(4.5 μ m)	W3(12 μ m)	W4(22 μ m)	70 μ m	100 μ m	160 μ m	250 μ m	350 μ m	500 μ m
(1)	(2)	(3)	(4)	(5)	(6)	(7)	(8)	(9)	(10)	(11)
A6	5.35E-01 (3.47E-02)	4.33E-01 (2.97E-02)	4.72E+00 (3.27E-01)	1.92E+01 (1.50E+00)	8.94E+01 (1.52E+01)	7.48E+01 (1.79E+01)	4.55E+01 (1.52E+01)
A7	1.04E+01 (6.27E-01)	5.90E+00 (3.56E-01)	1.28E+01 (7.90E-01)	1.24E+01 (1.36E+00)	2.81E+02 (2.35E+01)	1.31E+02 (1.58E+01)	5.22E+01 (1.24E+01)
A8	2.42E+00 (1.46E-01)	1.37E+00 (8.31E-02)	2.65E+00 (1.77E-01)	5.29E+00 (9.91E-01)	1.33E+02 (1.72E+01)	7.80E+01 (1.47E+01)	3.63E+01 (1.23E+01)
A9	6.61E+00 (3.98E-01)	4.28E+00 (2.59E-01)	1.37E+01 (8.28E-01)	4.19E+01 (2.71E+00)	2.34E+03 (1.67E+02)	...	2.24E+03 (1.64E+02)	8.95E+02 (6.33E+01)	3.39E+02 (2.53E+01)	1.08E+02 (1.06E+01)
A10	5.48E-01 (3.58E-02)	5.28E-01 (3.67E-02)	2.43E+00 (1.95E-01)	3.32E+00 (9.26E-01)	...	8.40E+01 (1.29E+01)	9.99E+01 (3.55E+01)	7.03E+01 (1.11E+01)	3.44E+01 (1.12E+01)	3.65E+01 (1.18E+01)
A11	1.01E+00 (6.49E-02)	8.11E-01 (5.21E-02)	2.23E+00 (1.58E-01)	6.72E+00 (7.53E-01)	4.24E+01 (7.20E+00)	4.15E+01 (1.27E+01)	3.40E+01 (1.02E+01)
A12	3.08E+00 (1.86E-01)	1.80E+00 (1.14E-01)	2.81E+00 (2.29E-01)	7.86E+00 (3.10E+00)	3.03E+01 (6.83E+00)	5.37E+01 (1.01E+01)	8.29E+01 (1.74E+01)	6.19E+01 (9.81E+00)	4.45E+01 (1.04E+01)	3.13E+01 (9.17E+00)

Note. (1) Object ID. R1-R11 are from Rowlands et al. (2015); EAH01-EAH18, EAS01-EAS15 and F34-F37 are from French et al. (2018a), and A1-A12 are from Alatalo et al. (2016a). (2)-(5) WISE fluxes. (6)-(11) Herschel fluxes. All fluxes are given in mJy. The total flux uncertainties, which correspond to 68% confidence levels, are given in parentheses when available. The data of EAS/EAH sources are presented in Smercina et al. (2018). No correction for extinction has been applied.

Table 4. Galaxy Properties

ID	r_{50}	$\log M_{\star}$	$\log M_{\text{dust}}$	$\log M_{\text{dust}}/M_{\star}$	$\log M_{\text{gas}}$	$\text{SFR}_{\text{uncor}}$	SFR_{cor}
(1)	(2)	(3)	(4)	(5)	(6)	(7)	(8)
R1	2.08	$9.82^{+0.24}_{-0.19}$	7.49 ± 0.07	-2.33 ± 0.23	< 8.50	6.74 ± 0.05	6.55 ± 0.06
R2	3.77	$10.63^{+0.06}_{-0.25}$	7.85 ± 0.02	-2.78 ± 0.15	9.71 ± 0.04	9.25 ± 0.05	8.97 ± 0.06
R3	1.41	$9.63^{+0.14}_{-0.12}$	6.89 ± 0.13	-2.74 ± 0.18	8.61 ± 0.14	6.42 ± 0.04	5.95 ± 0.06
R4	4.90	$10.28^{+0.17}_{-0.13}$	7.65 ± 0.11	-2.63 ± 0.19	9.80 ± 0.04	1.94 ± 0.02	2.17 ± 0.02
R5	1.95	$9.83^{+0.10}_{-0.08}$	7.39 ± 0.05	-2.44 ± 0.10	9.79 ± 0.02	3.15 ± 0.02	2.71 ± 0.03
R6	4.15	$10.44^{+0.09}_{-0.08}$	7.68 ± 0.14	-2.76 ± 0.16	9.58 ± 0.05	2.47 ± 0.02	1.86 ± 0.02
R7	1.92	$10.16^{+0.10}_{-0.08}$	7.02 ± 0.11	-3.14 ± 0.14	9.56 ± 0.07	1.05 ± 0.01	0.92 ± 0.01
R9	2.90	$10.28^{+0.09}_{-0.09}$	7.60 ± 0.10	-2.68 ± 0.13	9.66 ± 0.04	0.42 ± 0.01	0.39 ± 0.01
R10	4.72	$10.21^{+0.10}_{-0.09}$	7.58 ± 0.06	-2.63 ± 0.11	9.45 ± 0.05	0.98 ± 0.01	1.01 ± 0.01
EAH01	2.09	$10.45^{+0.12}_{-0.11}$	7.58 ± 0.02	-2.87 ± 0.12	9.71 ± 0.06	0.06 ± 0.01	0.01 ± 0.01
EAH02	1.71	$10.39^{+0.11}_{-0.10}$	6.64 ± 0.02	-3.75 ± 0.11	9.53 ± 0.09	0.03 ± 0.01	0.01 ± 0.01
EAH03	3.17	$10.34^{+0.11}_{-0.10}$	7.51 ± 0.02	-2.83 ± 0.11	9.80 ± 0.05	0.02 ± 0.01	< 0.003
EAH04	2.98	$10.18^{+0.11}_{-0.09}$	6.32 ± 0.12	-3.86 ± 0.16	8.56 ± 0.09	0.07 ± 0.01	0.02 ± 0.01
EAH05	1.42	$10.81^{+0.15}_{-0.13}$	7.54 ± 0.02	-3.27 ± 0.14	9.56 ± 0.09	0.06 ± 0.01	0.04 ± 0.01
EAH06	1.93	$10.12^{+0.13}_{-0.10}$	6.75 ± 0.10	-3.37 ± 0.15	< 9.00	0.37 ± 0.04	...
EAH07	3.69	$9.88^{+0.10}_{-0.07}$	6.75 ± 0.10	-3.13 ± 0.13	< 8.62	0.22 ± 0.02	...
EAH08	1.67	$10.07^{+0.11}_{-0.11}$	8.02 ± 0.12	-2.05 ± 0.16	9.15 ± 0.15	0.04 ± 0.01	...
EAH09	1.81	$11.01^{+0.11}_{-0.11}$	6.52 ± 0.11	-4.49 ± 0.16	8.50 ± 0.13	0.06 ± 0.01	0.01 ± 0.01
EAH10	1.22	$10.24^{+0.12}_{-0.08}$	7.72 ± 0.08	-2.52 ± 0.13	9.86 ± 0.12	0.04 ± 0.03	0.01 ± 0.01
EAH11	1.09	$10.64^{+0.10}_{-0.09}$	6.33 ± 0.15	-4.31 ± 0.18	< 9.19	0.17 ± 0.02	...
EAH12	0.96	$9.89^{+0.12}_{-0.10}$	6.40 ± 0.03	-3.49 ± 0.11	< 9.42	0.18 ± 0.03	0.05 ± 0.02

Table 4 continued

Table 4 (continued)

ID	r_{50}	$\log M_{\star}$	$\log M_{\text{dust}}$	$\log M_{\text{dust}}/M_{\star}$	$\log M_{\text{gas}}$	SFR _{uncor}	SFR _{cor}
	(arcsec)	(M_{\odot})	(M_{\odot})		(M_{\odot})	($M_{\odot} \text{ yr}^{-1}$)	($M_{\odot} \text{ yr}^{-1}$)
(1)	(2)	(3)	(4)	(5)	(6)	(7)	(8)
EAH13	1.50	11.00 ^{+0.13} _{-0.11}	7.64±0.19	-3.36±0.22	9.89±0.08	0.62±0.14	...
EAH14	1.18	10.04 ^{+0.13} _{-0.10}	5.96±0.24	-4.08±0.27	<9.25	0.10±0.01	0.01±0.01
EAH15	1.52	10.40 ^{+0.13} _{-0.12}	6.44±0.22	-3.96±0.25	<9.04	0.06±0.01	0.01±0.01
EAH16	1.37	10.74 ^{+0.09} _{-0.07}	6.94±0.46	-3.80±0.47	<9.79	0.51±0.09	...
EAH17	1.49	10.05 ^{+0.10} _{-0.10}	6.80±0.32	-3.25±0.34	<9.01	0.05±0.01	0.02±0.01
EAH18	3.33	10.38 ^{+0.12} _{-0.10}	5.78±0.18	-4.60±0.21	8.68±0.15	0.03±0.01	< 0.001
EAS01	4.39	10.24 ^{+0.12} _{-0.11}	5.32±0.10	-4.92±0.15	<8.40	0.01±0.01	< 0.0004
EAS02	3.72	10.37 ^{+0.10} _{-0.10}	6.27±0.14	-4.10±0.17	8.71±0.13	0.03±0.01	0.01±0.01
EAS03	2.34	10.34 ^{+0.10} _{-0.09}	7.20±0.14	-3.14±0.17	9.76±0.06	0.17±0.02	0.02±0.01
EAS04	3.12	9.99 ^{+0.11} _{-0.10}	5.43±0.16	-4.56±0.19	<7.74	0.01±0.01	...
EAS05	2.74	11.33 ^{+0.10} _{-0.10}	7.09±0.10	-4.24±0.14	9.09±0.14	0.11±0.02	0.04±0.01
EAS06	2.91	10.14 ^{+0.09} _{-0.09}	6.61±0.08	-3.53±0.12	9.23±0.04	0.06±0.01	0.03±0.01
EAS07	2.34	10.54 ^{+0.12} _{-0.11}	5.90±1.04	-4.64±1.05	8.64	0.04±0.02	< 0.01
EAS08	4.25	10.67 ^{+0.10} _{-0.10}	6.41±0.88	-4.26±0.89	<8.60	0.05±0.03	< 0.01
EAS09	3.27	10.56 ^{+0.11} _{-0.10}	6.88±0.03	-3.68±0.11	9.12±0.06	0.04±0.01	0.01±0.01
EAS10	2.03	10.53 ^{+0.12} _{-0.10}	5.64±0.03	-4.89±0.11	<8.79	0.02±0.01	...
EAS11	3.04	10.71 ^{+0.14} _{-0.13}	6.59±0.12	-4.12±0.18	<8.84	0.08±0.02	0.02±0.01
EAS12	6.39	10.80 ^{+0.10} _{-0.11}	7.33±0.17	-3.47±0.20	8.54±0.14	0.03±0.01	...
EAS13	3.80	10.95 ^{+0.10} _{-0.10}	7.50±0.33	-3.45±0.34	<9.12	0.09±0.02	< 0.02
EAS14	3.72	11.31 ^{+0.11} _{-0.11}	7.49±0.24	-3.82±0.26	9.70±0.09	0.41±0.07	...
EAS15	2.82	10.83 ^{+0.10} _{-0.09}	6.88±0.21	-3.95±0.23	9.08±0.14	0.17±0.05	< 0.07
F34	1.77	10.20 ^{+0.12} _{-0.11}	8.40±0.08	-1.80±0.14	9.83±0.15	0.03±0.01	0.01±0.01
F35	2.73	10.64 ^{+0.10} _{-0.09}	8.18±0.06	-2.46±0.11	9.80±0.15	0.08±0.01	0.04±0.01
F36	1.11	10.28 ^{+0.13} _{-0.13}	7.33±0.24	-2.95±0.27	9.32±0.15	0.61±0.13	...
F37	3.33	10.38 ^{+0.12} _{-0.10}	6.26±0.24	-4.12±0.26	8.82±0.15	0.03±0.01	< 0.001
A1	2.18	10.64 ^{+0.10} _{-0.09}	7.86±0.32	-2.78±0.33	9.57±0.15	3.89±0.09	0.51±0.21
A2	5.38	9.98 ^{+0.35} _{-0.53}	7.89±0.26	-2.09±0.51	9.59±0.15	0.35±0.01	0.36±0.01
A3	2.70	11.30 ^{+0.10} _{-0.10}	8.89±0.19	-2.41±0.21	10.06±0.15	14.25±0.44	3.19±0.54
A4	1.11	10.79 ^{+0.06} _{-0.05}	8.47±0.18	-2.32±0.19	9.86±0.15	27.71±0.90	12.04±1.29
A5	6.41	10.19 ^{+0.09} _{-0.10}	8.07±0.04	-2.12±0.10	9.40±0.08	0.13±0.01	0.02±0.01
A6	1.77	10.34 ^{+0.10} _{-0.09}	7.99±0.13	-2.35±0.16	9.63±0.15	7.04±0.08	6.17±0.12
A7	7.41	10.80 ^{+0.10} _{-0.11}	7.82±0.14	-2.98±0.18	9.55±0.15	0.19±0.01	0.05±0.01
A8	5.43	10.15 ^{+0.10} _{-0.09}	7.56±0.21	-2.59±0.23	9.43±0.15	0.14±0.01	0.05±0.01
A9	4.40	10.59 ^{+0.10} _{-0.09}	7.80±0.02	-2.79±0.10	9.54±0.15	1.13±0.02	0.61±0.03
A10	2.62	10.65 ^{+0.10} _{-0.10}	8.19±0.19	-2.46±0.21	9.73±0.15	1.04±0.03	0.78±0.05
A11	1.51	10.00 ^{+0.11} _{-0.11}	8.19±0.19	-1.81±0.22	9.01±0.11	0.19±0.01	0.04±0.01
A12	2.66	10.51 ^{+0.13} _{-0.11}	7.68±0.30	-2.83±0.32	8.86±0.06	0.22±0.01	0.05±0.01

Note. (1) Object ID. (2) Petrosian radius from SDSS 14th Data Release (DR14, Abolfathi et al. 2018; containing 50% light). (3) Stellar masses from the SDSS MPA-JHU (Brinchmann et al. 2004; Tremonti et al. 2004) catalog. (4) CIGALE-derived dust masses. (5) Specific dust masses. (6) Molecular gas masses from French et al. (2015), Alatalo et al. (2016b), or converted from dust masses if no CO measurement is available (with an estimated uncertainty of 0.15 dex). (7) Star formation rates derived from H α fluxes from the MPA-JHU catalog (corrected for internal dust extinction). (8) Star formation rates corrected for AGN contribution.

REFERENCES

- Abolfathi, B., Aguado, D. S., Aguilar, G., et al. 2018, The Astrophysical Journal Supplement Series, 235, 42
- Agius, N. K., Sansom, A. E., Popescu, C. C., et al. 2013, MNRAS, 431, 1929
- Aihara, H., Allende Prieto, C., An, D., et al. 2011, ApJS, 193, 29

- Alatalo, K., Cales, S. L., Rich, J. A., et al. 2016a, *ApJS*, 224, 38
- Alatalo, K., Lisenfeld, U., Lanz, L., et al. 2016b, *ApJ*, 827, 106
- Baldwin, J. A., Phillips, M. M., & Terlevich, R. 1981, *Publications of the Astronomical Society of the Pacific*, 93, 5
- Balog, Z., Müller, T., Nielbock, M., et al. 2014, *Experimental Astronomy*, 37, 129
- Baron, D., Netzer, H., Poznanski, D., Prochaska, J. X., & Förster Schreiber, N. M. 2017, *MNRAS*, 470, 1687
- Baron, D., Netzer, H., Prochaska, J. X., et al. 2018, *MNRAS*, 480, 3993
- Blanton, M. R., & Roweis, S. 2007, *AJ*, 133, 734
- Bolatto, A. D., Wolfire, M., & Leroy, A. K. 2013, *Annual Review of Astronomy and Astrophysics*, 51, 207
- Boquien, M., Burgarella, D., Roehlly, Y., et al. 2019, *A&A*, 622, A103
- Brinchmann, J., Charlot, S., White, S. D. M., et al. 2004, *MNRAS*, 351, 1151
- Bruzual, G., & Charlot, S. 2003, *MNRAS*, 344, 1000
- Bundy, K., Bershady, M. A., Law, D. R., et al. 2015, *ApJ*, 798, 7
- Buyle, P., Michielsen, D., De Rijcke, S., et al. 2006, *ApJ*, 649, 163
- Calzetti, D., Armus, L., Bohlin, R. C., et al. 2000, *ApJ*, 533, 682
- Cappellari, M., Scott, N., Alatalo, K., et al. 2013, *MNRAS*, 432, 1709
- Chabrier, G. 2003, *PASP*, 115, 763
- Chang, T.-C., van Gorkom, J. H., Zabludoff, A. I., Zaritsky, D., & Mihos, J. C. 2001, *AJ*, 121, 1965
- Cicone, C., Maiolino, R., Sturm, E., et al. 2014, *A&A*, 562, A21
- Ciesla, L., Boselli, A., Smith, M. W. L., et al. 2012, *A&A*, 543, A161
- Couch, W. J., & Sharples, R. M. 1987, *MNRAS*, 229, 423
- Cutri, R. M., Mainzer, A., Conrow, T., et al. 2015, *Explanatory Supplement to the NEOWISE Data Release Products*, Tech. rep.
- da Cunha, E., Charlot, S., & Elbaz, D. 2008, *MNRAS*, 388, 1595
- da Cunha, E., Eminian, C., Charlot, S., & Blaizot, J. 2010, *MNRAS*, 403, 1894
- Dale, D. A., Cohen, S. A., Johnson, L. C., et al. 2009, *ApJ*, 703, 517
- Dale, D. A., Aniano, G., Engelbracht, C. W., et al. 2012, *ApJ*, 745, 95
- Davis, T. A., Young, L. M., Crocker, A. F., et al. 2014, *MNRAS*, 444, 3427
- Draine, B. T., & Li, A. 2007, *ApJ*, 657, 810
- Dressler, A., & Gunn, J. E. 1983, *ApJ*, 270, 7
- French, K. D., Yang, Y., Zabludoff, A., et al. 2015, *ApJ*, 801, 1
- French, K. D., Yang, Y., Zabludoff, A. I., & Tremonti, C. A. 2018a, *ApJ*, 862, 2
- French, K. D., Zabludoff, A. I., Yoon, I., et al. 2018b, *ApJ*, 861, 123
- Gallazzi, A., Charlot, S., Brinchmann, J., White, S. D. M., & Tremonti, C. A. 2005, *MNRAS*, 362, 41
- Gao, Y., & Solomon, P. M. 2004, *ApJ*, 606, 271
- Hayward, C. C., Lanz, L., Ashby, M. L. N., et al. 2014, *MNRAS*, 445, 1598
- Isobe, T., Feigelson, E. D., & Nelson, P. I. 1986, *ApJ*, 306, 490
- Jarrett, T. H., Chester, T., Cutri, R., et al. 2000, *AJ*, 119, 2498
- Jarrett, T. H., Masci, F., Tsai, C. W., et al. 2012, *AJ*, 144, 68
- Kelly, B. C. 2007, *ApJ*, 665, 1489
- Kennicutt, Jr., R. C. 1998, *ApJ*, 498, 541
- Kennicutt, Jr., R. C., Tamblyn, P., & Congdon, C. E. 1994, *ApJ*, 435, 22
- Lanz, L., Hickox, R. C., Baloković, M., et al. 2019, *ApJ*, 870, 26
- Lavalley, M., Isobe, T., & Feigelson, E. 1992, in *Astronomical Society of the Pacific Conference Series*, Vol. 25, *Astronomical Data Analysis Software and Systems I*, ed. D. M. Worrall, C. Biemesderfer, & J. Barnes, 245
- Leroy, A. K., Walter, F., Sandstrom, K., et al. 2013, *AJ*, 146, 19
- Mainzer, A., Bauer, J., Grav, T., et al. 2011, *ApJ*, 731, 53
- Marton, G., Calzoletti, L., Perez Garcia, A. M., et al. 2017, *ArXiv e-prints*, arXiv:1705.05693
- Morrissey, P., Conrow, T., Barlow, T. A., et al. 2007, *ApJS*, 173, 682
- Noll, S., Burgarella, D., Giovannoli, E., et al. 2009, *A&A*, 507, 1793
- Norton, S. A., Gebhardt, K., Zabludoff, A. I., & Zaritsky, D. 2001, *ApJ*, 557, 150
- O'Donnell, J. E. 1994, *ApJ*, 422, 158
- Pawlik, M. M., Wild, V., Walcher, C. J., et al. 2016, *MNRAS*, 456, 3032
- Planck Collaboration, Ade, P. A. R., Aghanim, N., et al. 2016, *A&A*, 594, A13
- Pracy, M. B., Croom, S., Sadler, E., et al. 2013, *MNRAS*, 432, 3131
- Rowlands, K., Wild, V., Nesvadba, N., et al. 2015, *MNRAS*, 448, 258
- Rowlands, K., Dunne, L., Maddox, S., et al. 2012, *MNRAS*, 419, 2545
- Rowlands, K., Dunne, L., Dye, S., et al. 2014, *MNRAS*, 441, 1017
- Schulz, B., Marton, G., Valtchanov, I., et al. 2017, *ArXiv e-prints*, arXiv:1706.00448
- Skrutskie, M. F., Cutri, R. M., Stiening, R., et al. 2006, *AJ*, 131, 1163
- Smercina, A., Smith, J. D. T., Dale, D. A., et al. 2018, *ApJ*, 855, 51
- Snyder, G. F., Cox, T. J., Hayward, C. C., Hernquist, L., & Jonsson, P. 2011, *ApJ*, 741, 77
- Tran, K.-V. H., Franx, M., Illingworth, G. D., et al. 2004, *ApJ*, 609, 683
- Tremonti, C. A., Heckman, T. M., Kauffmann, G., et al. 2004, *ApJ*, 613, 898
- Veilleux, S., & Osterbrock, D. E. 1987, *The Astrophysical Journal Supplement Series*, 63, 295

- Wild, V., Almaini, O., Dunlop, J., et al. 2016, MNRAS, 463, 832
- Wild, V., Heckman, T., & Charlot, S. 2010, MNRAS, 405, 933
- Wong, O. I., Schawinski, K., Kaviraj, S., et al. 2012, MNRAS, 420, 1684
- Yang, Y., Zabludoff, A. I., Zaritsky, D., Lauer, T. R., & Mihos, J. C. 2004, ApJ, 607, 258
- Yang, Y., Zabludoff, A. I., Zaritsky, D., & Mihos, J. C. 2008, ApJ, 688, 945
- Zabludoff, A. I., Zaritsky, D., Lin, H., et al. 1996, ApJ, 466, 104
- Zwaan, M. A., Kuntschner, H., Pracy, M. B., & Couch, W. J. 2013, MNRAS, 432, 492

APPENDIX

A. MINIMAL *HERSCHEL* DATA REQUIRED FOR RELIABLE M_{dust}

According to [Draine & Li \(2007\)](#), determining the position of the FIR SED peak is crucial for obtaining a reliable M_{dust} . Here we determine the fewest and best bands for fitting the SEDs of our sample. We perform SED fitting tests using 12 EAH/EAS PSBs (i.e., EAH01-07, EAH09-10, EAS05-06, and EAS09) that have archival fluxes in all six *Herschel* bands and that are best fit by the model at 70 and 100 μm . Then, we remove different sets of bands, refit the SEDs of these galaxies, and compare the derived M_{dust} with those derived from fitting all six *Herschel* bands. As shown in Figure 9, 70 μm +100 μm +160 μm or 250 μm +350 μm +500 μm bands are enough to derive reliable M_{dust} , while outliers exist where only 70 μm +100 μm or 250 μm +350 μm bands are used¹⁶. To be conservative, we remove all the PSBs with <3 *Herschel* bands and include only those 58 PSBs with at least three *Herschel* measurements in our analysis in this paper.

B. EFFECT OF INCLUDING UV AND OPTICAL DATA ON M_{dust}

We also test the effects of fitting the SEDs for 33 PSBs (i.e., EAH01-18 and EAS01-15) from the UV to FIR using CIGALE, as we do in this paper, compared to only fitting with MIR-FIR data on M_{dust} . As shown in Figure 10, M_{dust} is very robust whether or not we use UV and optical data in our fitting. This is expected, as M_{dust} is basically determined by the position and height of the IR peak.

C. M_{dust} COMPARISON WITH SMERCINA ET AL. (2018)

[Smircina et al. \(2018\)](#) derive M_{dust} for 33 PSBs (i.e., EAH01-18 and EAS01-15) by performing SED fitting using the DL07 model and a $T = 5000$ K blackbody stellar model. To compare our results with theirs, we combine the *WISE* and *Herschel* fluxes from [Smircina et al. \(2018\)](#) with our UV-optical fluxes and perform SED fitting using CIGALE. As shown in Figure 11, when the error bars are taken into account, the M_{dust} 's are consistent¹⁷ in almost all cases: 32/33 PSBs have $-0.5 M_{\odot} < \Delta \log M_{\text{dust}} < 0.25 M_{\odot}$, with on average $\Delta \log M_{\text{dust}} = -0.04_{-0.04}^{+0.05} M_{\odot}$. The small differences in M_{dust} and its error bars arise mostly from differences in our model assumptions and in our definitions of χ^2 .

D. EFFECT OF BURST AGES ON M_{dust}

We find a discrepancy between the (post-)burst ages derived from CIGALE and [French et al. \(2018a\)](#), who perform age-dating by combining *GALEX* photometry, SDSS photometry, and SDSS spectra. We have tested two types of $\text{age}_{\text{burst}}$ priors for CIGALE: one is the full range described in Table 1, the other is restricted to the $2\text{-}\sigma$ value ranges provided in [French et al. \(2018a\)](#) for our total sample of 58 PSBs. As shown in Figure 12a, even provided with a full range of priors, the average of the (post-)burst ages from CIGALE is still higher than that from [French et al. \(2018a\)](#) (0.55 versus 0.30 Gyr), with a larger standard deviation (0.59 versus 0.20 Gyr). Having excluded all other possible factors that may contribute to such discrepancy (models, priors, and photometric data), we conclude that it is the inclusion of optical spectral information that causes the difference. As illustrated in Figure 12b, for a subsample of PSBs in [French et al. \(2018a\)](#), the (post-)burst ages derived by fitting with only photometry (y-axis) are systematically higher and have larger scatter than those derived by fitting photometry and spectral lines together (x-axis) using the age-dating method in [French et al. \(2018a\)](#). This age discrepancy almost has no impact on M_{dust} , however, as shown in Figure 12c. The decreasing trend of M_{dust} versus $\text{age}_{(\text{post-})\text{burst}}$ is also not notably affected. The age-dating from [French et al. \(2018a\)](#) is likely more accurate, so we adopt the [French et al. \(2018a\)](#) PSB ages throughout this paper when considering the evolution of PSB properties.

E. SED FITS OF ALL 58 PSBS IN OUR SAMPLE

Here we present all 58 SED fits of our sample, eight of which are already presented in Figure 1.

¹⁶ If we loosen our criterion to ≤ 2 *Herschel* bands, 18 additional PSBs could be included, the majority of which have 70 μm +100 μm or 250 μm +350 μm bands. As our tests show that 70 μm +100 μm or 250 μm +350 μm bands are not enough to yield a reliable M_{dust} , we decide not to include them in our sample.

¹⁷ The $\log M_{\text{dust}}$ for EAH03 in [Smircina et al. \(2018\)](#) should be $7.55 M_{\odot}$, instead of $8.70 M_{\odot}$. We thank A. Smircina and D. A. Dale for their help in identifying this problem.

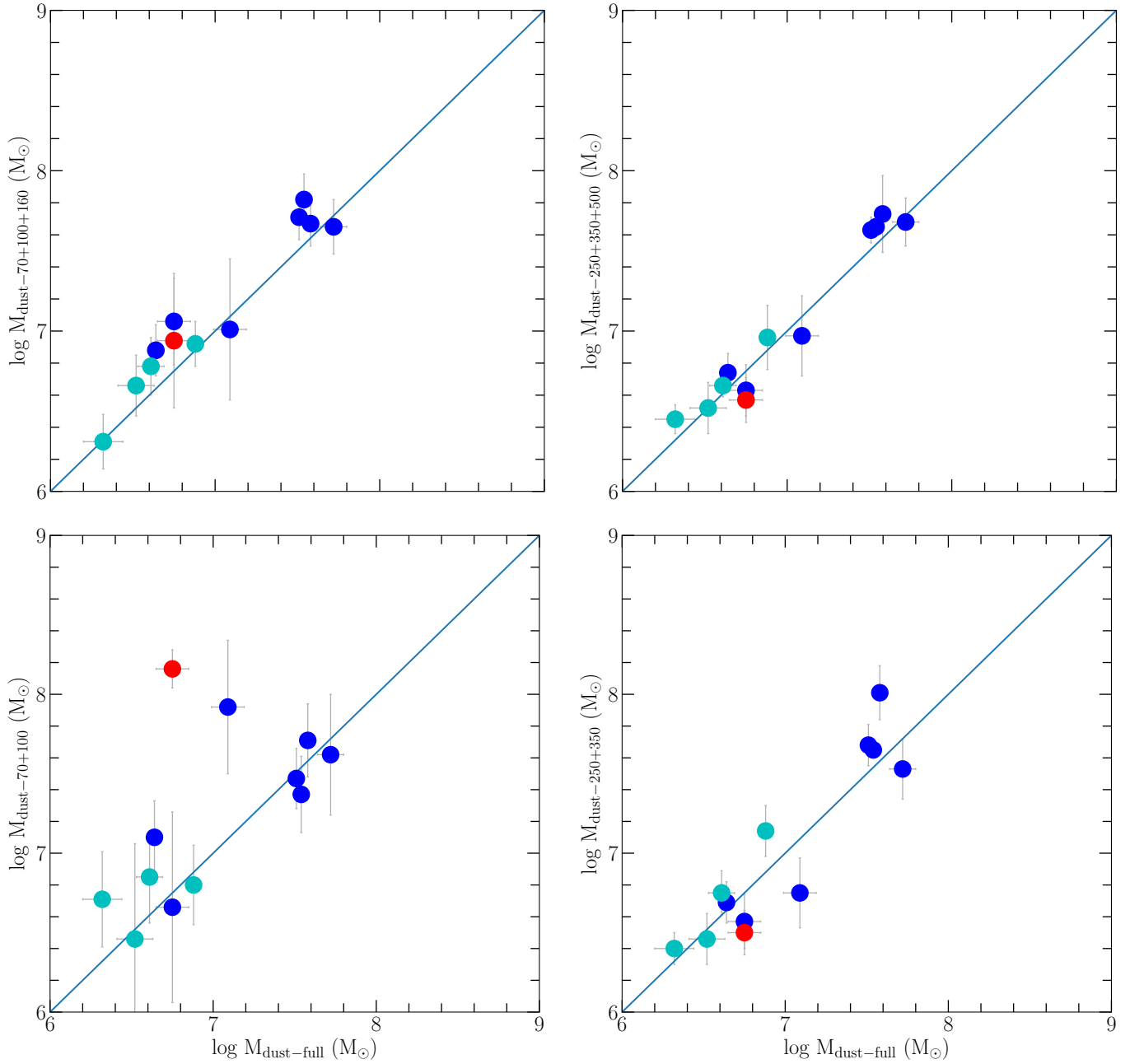


Figure 9. Comparison of M_{dust} derived by CIGALE using different *Herschel* bands. The x-axis includes all six *Herschel* bands and the y-axis includes different subsets of *Herschel* bands. Different colors represent different redshift ranges (cyan: $z \leq 0.03$; red: $0.03 < z \leq 0.04$; blue: $z > 0.04$). All error bars (shown in gray) correspond to 68% confidence levels. The one-to-one line is plotted in blue for comparison. It can be seen that $70 \mu\text{m}+100 \mu\text{m}+160 \mu\text{m}$ or $250 \mu\text{m}+350 \mu\text{m}+500 \mu\text{m}$ bands are enough to derive reliable M_{dust} , while outliers exist where only $70 \mu\text{m}+100 \mu\text{m}$ or $250 \mu\text{m}+350 \mu\text{m}$ bands are used.

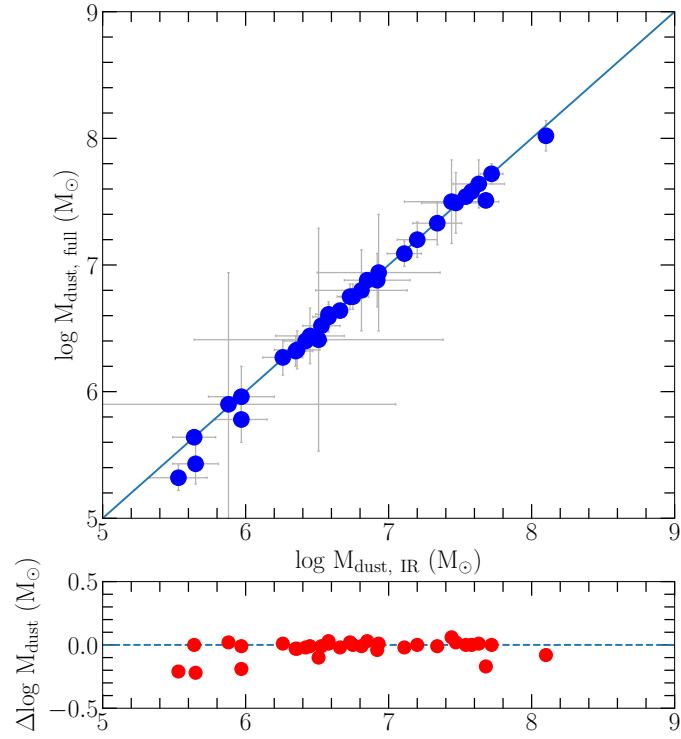


Figure 10. Comparison of M_{dust} derived by CIGALE by fitting only the MIR-FIR SED (x -axis) versus the full UV-FIR SED (y -axis), with the difference in M_{dust} ($y-x$) plotted in the bottom panel. All error bars (shown in gray) correspond to 68% confidence levels. The one-to-one solid line (upper) and the zero fiducial dashed line (lower) are plotted in blue for comparison. The M_{dust} is very robust whether or not we use UV and optical data in our fitting.

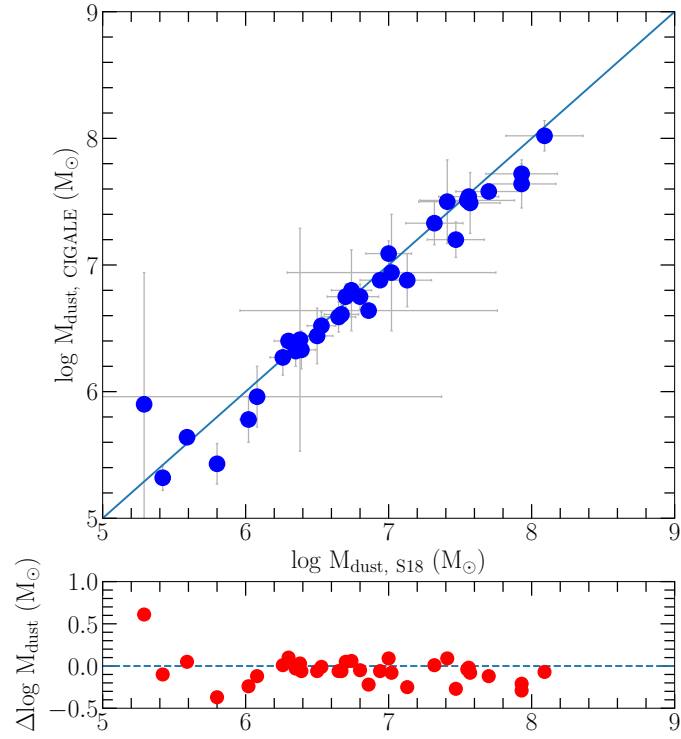


Figure 11. Comparison of M_{dust} derived by us using CIGALE (y-axis) and by [Smercina et al. \(2018\)](#) using an alternate stellar model (x-axis), with the difference in M_{dust} (y-x) plotted at the bottom. All error bars (shown in gray) correspond to 68% confidence levels. The one-to-one solid line (upper) and the zero fiducial dashed line (lower) are plotted in blue for comparison. When the error bars are taken into account, the M_{dust} 's are consistent in almost all cases.

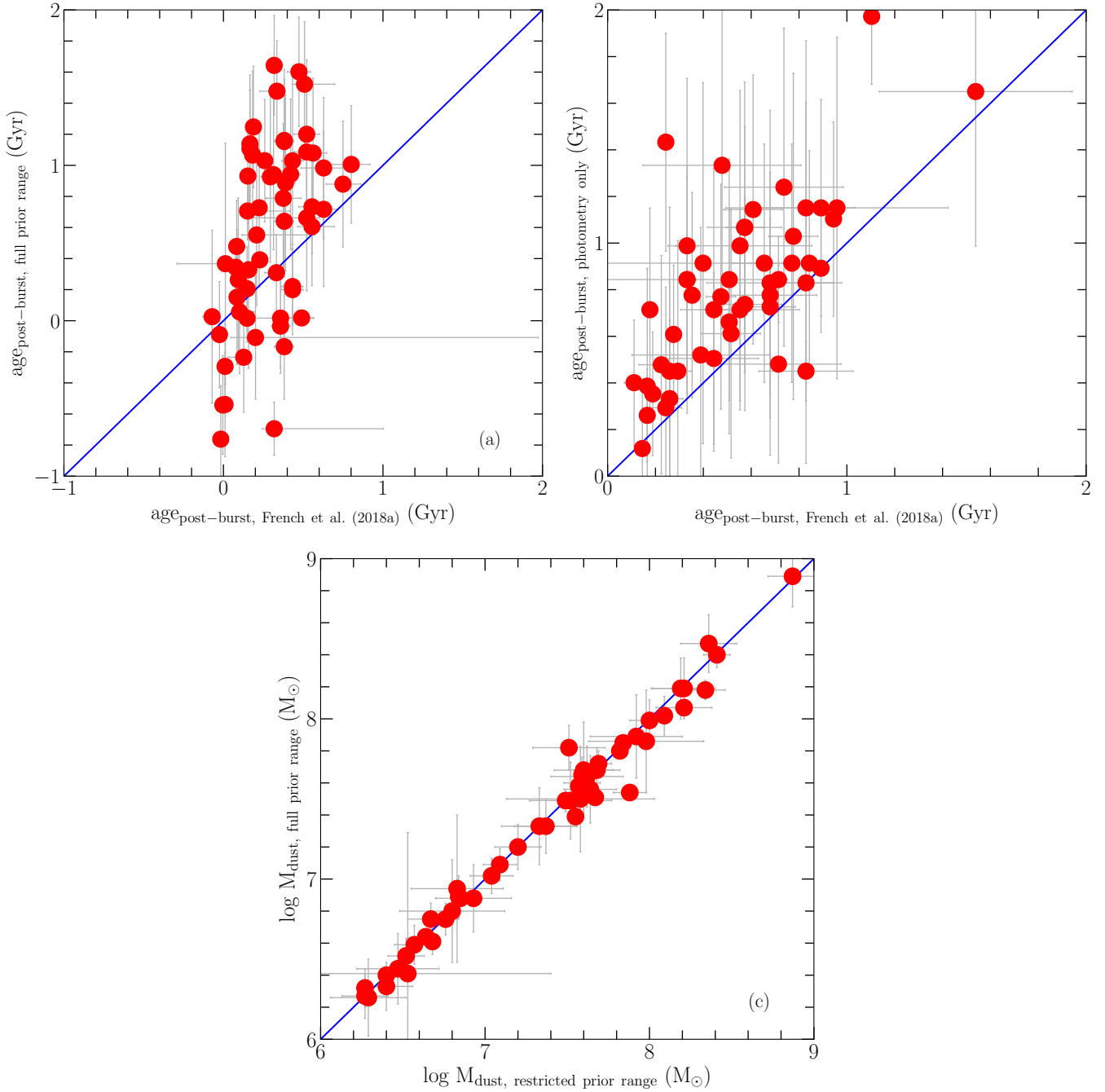


Figure 12. Quantifying the effects of priors on post-burst age and M_{dust} . We see from (a) that the post-burst ages derived from our CIGALE fits without restricted prior ranges have more scatter and are on average higher than the ages from French et al. (2018a), where optical spectral lines are included in the fits. From (b), using the age-dating method in French et al. (2018a), we see this effect of adding those optical spectral lines into age-dating. Nevertheless, from (c) we see that M_{dust} is robust to the choice of priors.

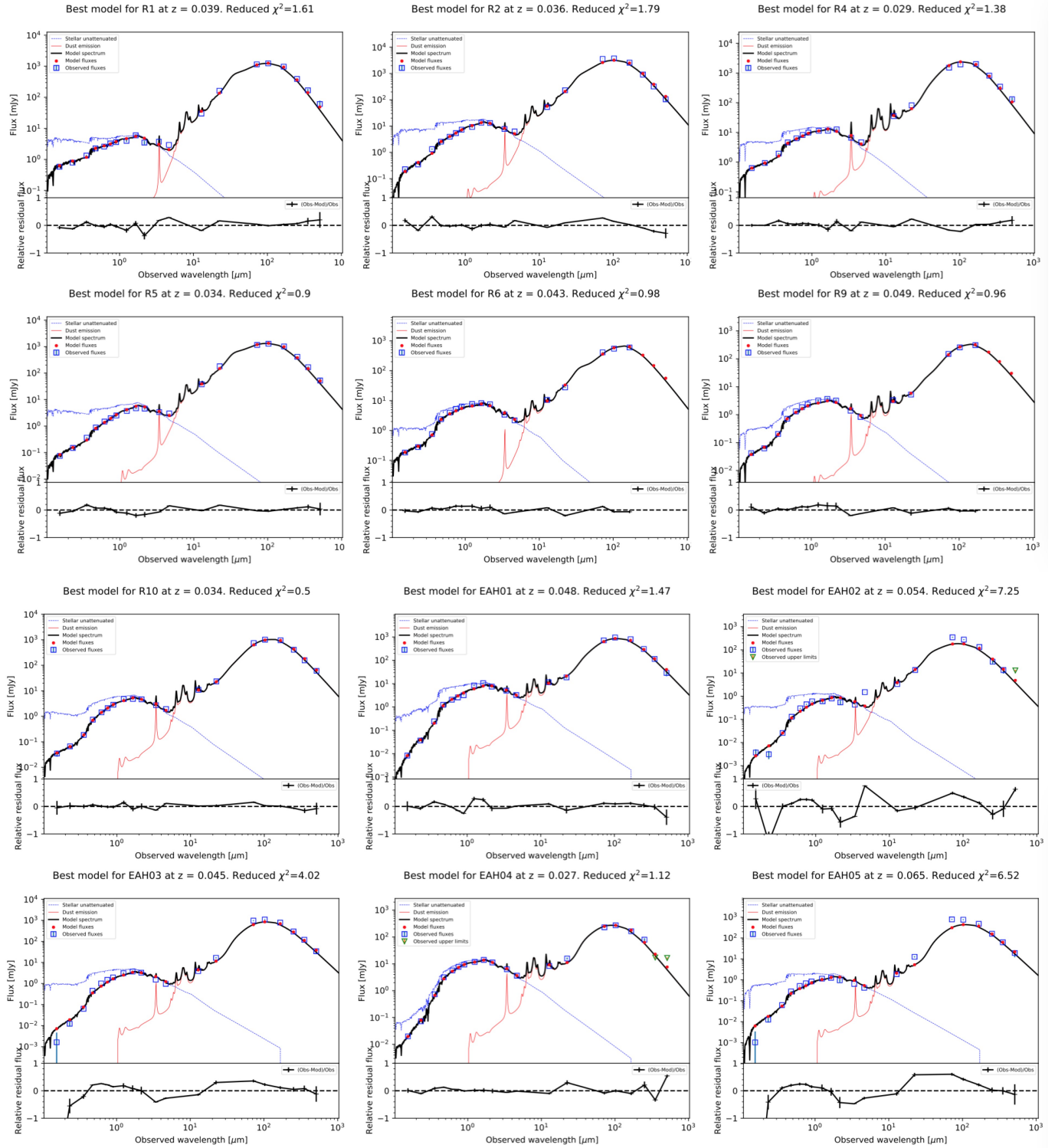


Figure 13a. All 58 SED fits of our sample derived from CIGALE (eight of them are already presented in Figure 1).

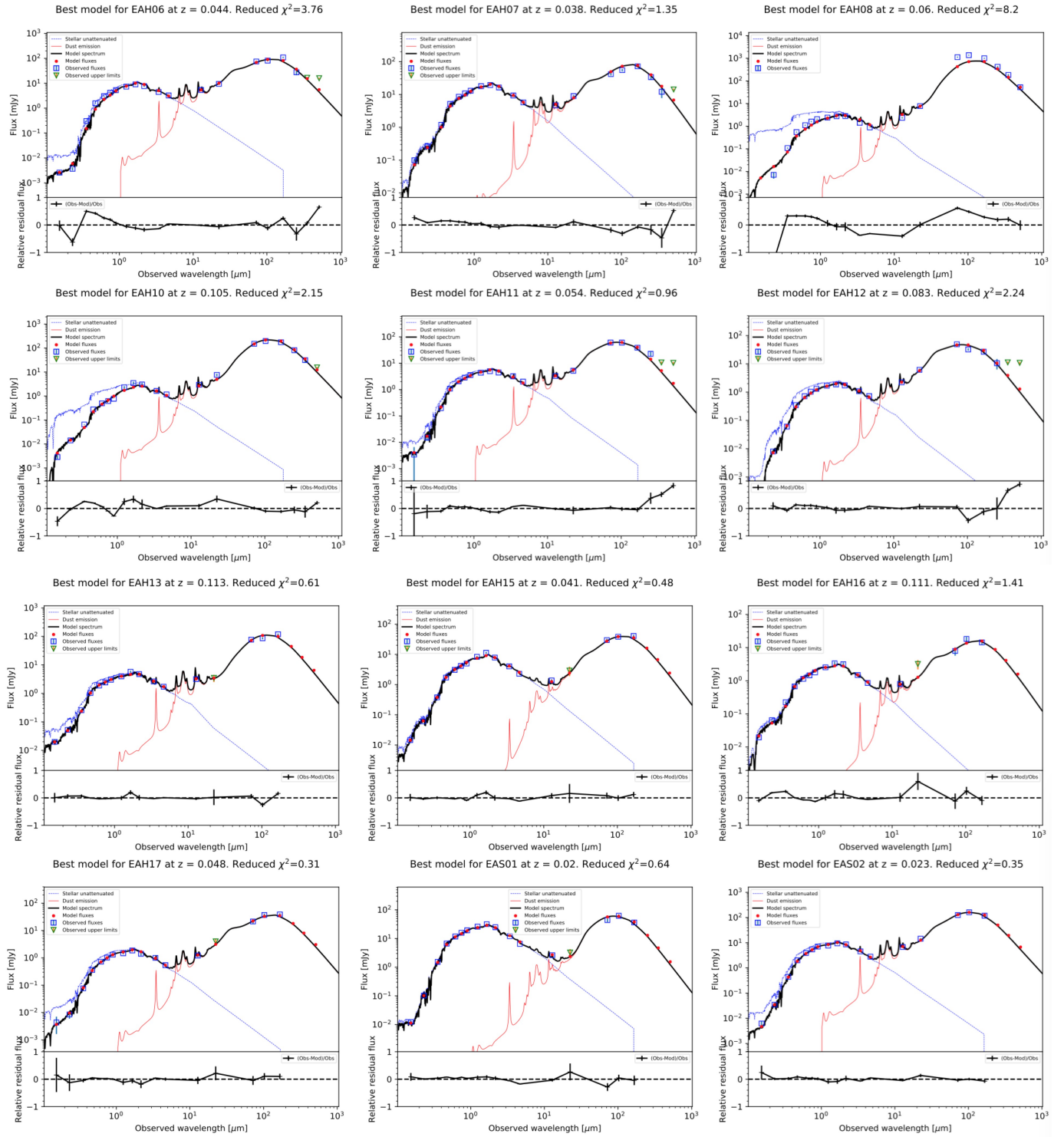


Figure 13b. Continued.

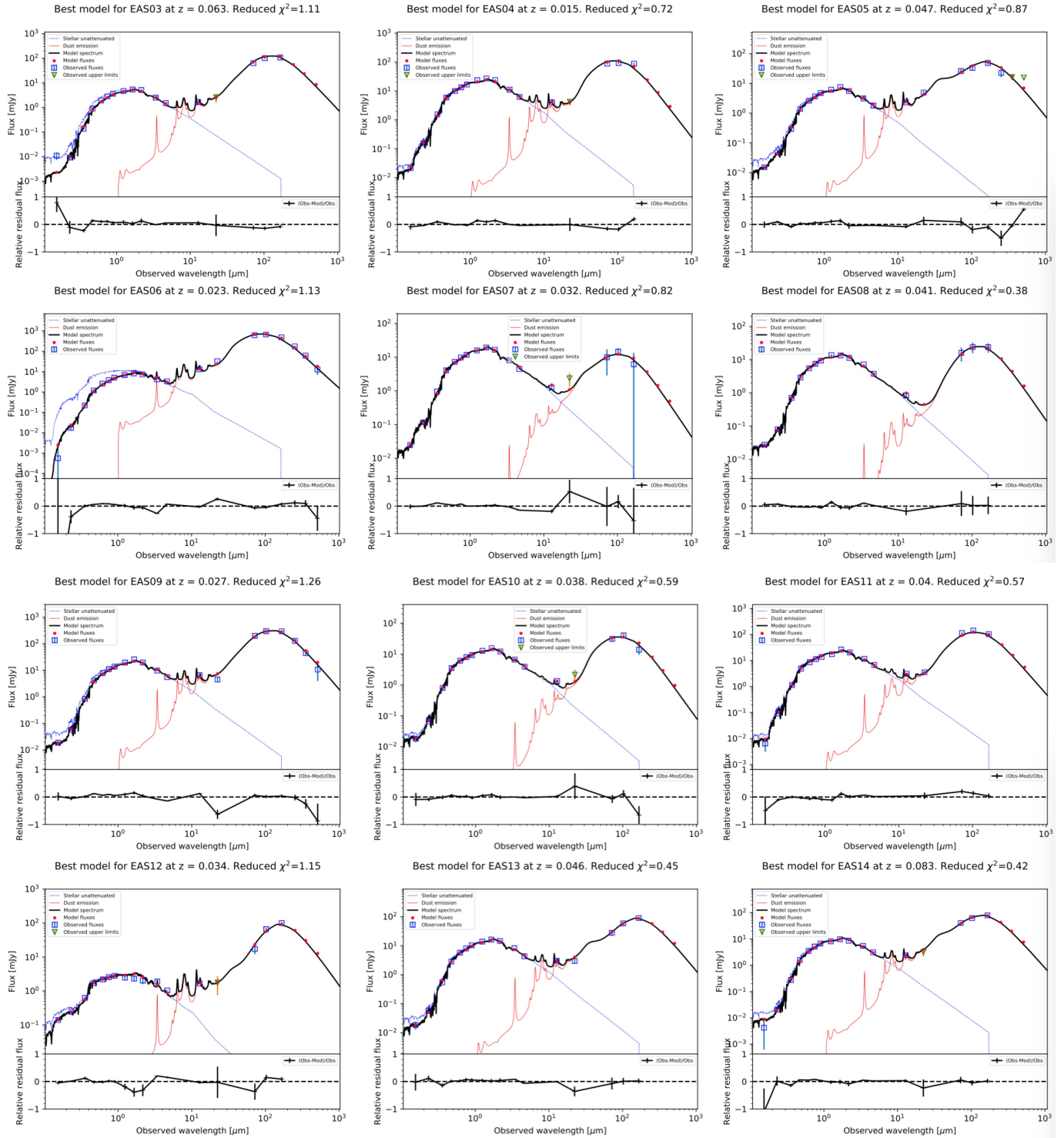


Figure 13c. Continued.

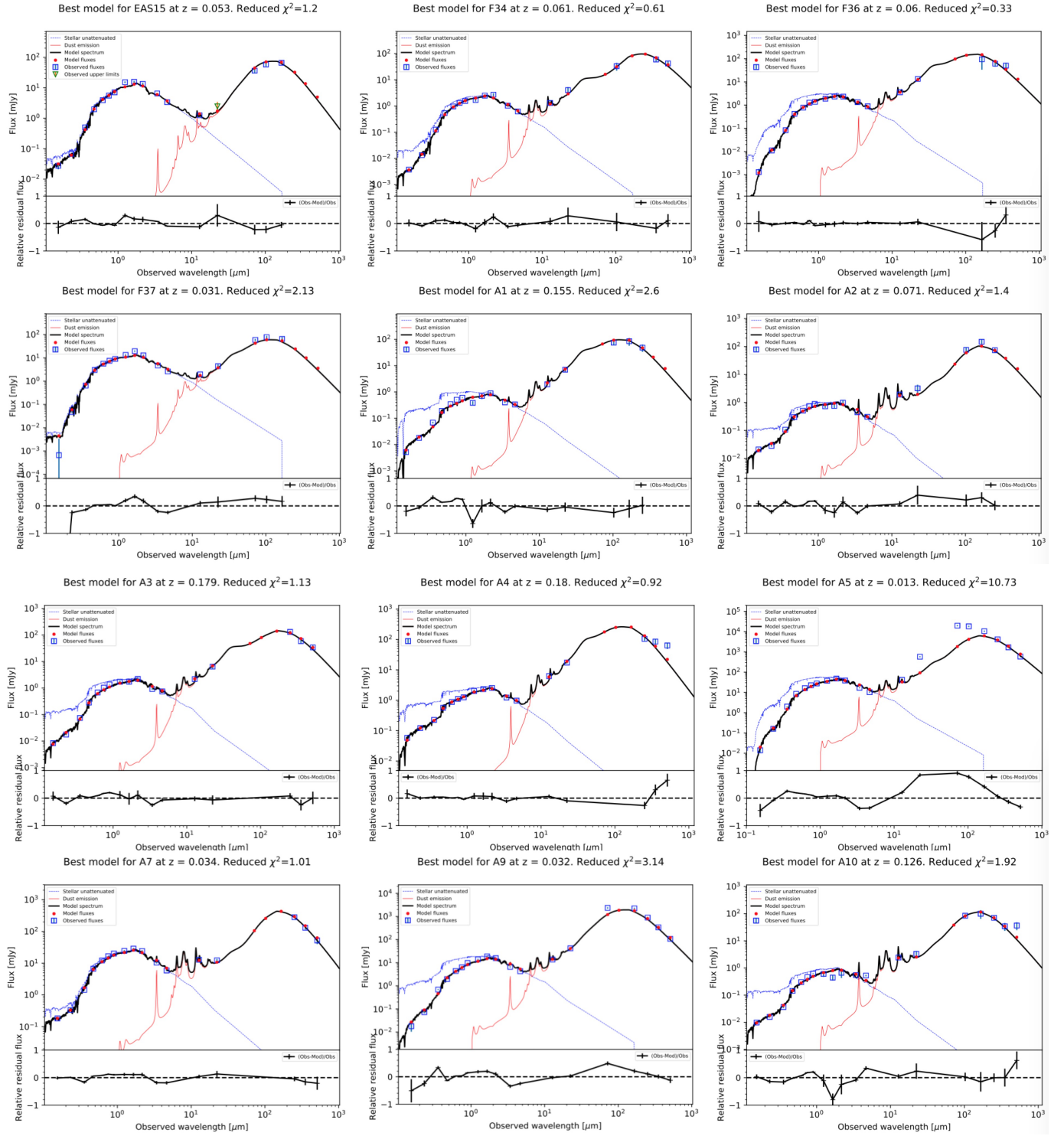
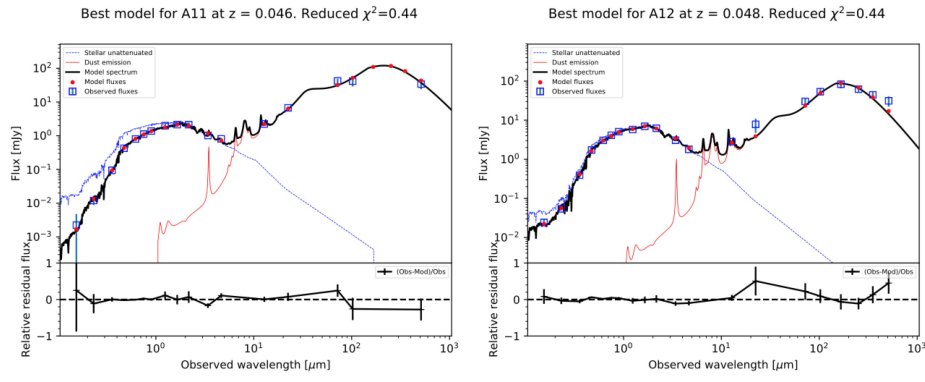


Figure 13d. Continued. The worst fit here, A5, is particularly extended ($r_{50} = 16$ arcsec) and dusty.

**Figure 13e. Continued.**